A COMPARISON OF THEORETICAL AND OBSERVED RADIANCES FROM NON-PRECIPITATING CUMULUS CLOUDS

MARK DEMARIA and THOMAS MCKEE

Atmospheric Scien
PAPER NO.
313

US ISSN 0067-0340

DEPARTMENT OF ATMOSPHERIC SCIENCE
COLORADO STATE UNIVERSITY
FORT COLLINS, COLORADO

A COMPARISON OF THEORETICAL AND OBSERVED RADIANCES FROM NON-PRECIPITATING CUMULUS CLOUDS

by

Mark DeMaria and Thomas McKee

This research was supported by the
Global Atmospheric Research Program,
National Science Foundation, and
the GATE Project Office, NOAA under
Grant No. ATM76-80568.

Department of Atmospheric Science
Colorado State University
Fort Collins, Colorado
80523

June, 1979

Atmospheric Science Paper No. 313

ABSTRACT

Relative radiances from a theoretical model for the scattering of solar radiation by finite clouds were compared to observed radiances from the sides of non-precipitating cumulus clouds. The sides of 5 cumulus clouds ranging from 1-3 km in depth with width to depth ratios of about 1.5 were scanned with an aircraft mounted radiometer sensitive in the spectral range of 0.65 to 0.95 μm. Photographs of each cloud were taken just before each scan with a camera optically aligned with the radiometer. The theoretical model uses the Monte Carlo method of radiative transfer for finite clouds in the shape of rectangular parallelepipeds. The radiometer field of view intercepted a circular spot with a diameter of about 1/20 of the cloud height. On this scale the radiometer scans were strongly affected by small scale cloud features so that the model radiances which are averages over a smooth cloud face did not compare well. A linear regression between the model and actual relative radiances resulted in a correlation coefficient (r) of only 0.47. When each scan was averaged, the smaller scale cloud features became less important. A linear regression for scan averages resulted in a correlation coefficient of 0.64. On this scale, the model calculations were verified by the observations except for a few observations where smaller scale cloud features and model cloud corners were important. Elimination of the data points related to cloud features not contained in the model resulted in a correlation coefficient of 0.86. When several successive scans were averaged together, the correlation coefficient increased to 0.91.

On this scale, the effects of the smaller scale cloud features and model cloud corners became noticeably less important.

The variability in relative radiance from the sides of the clouds was also studied. An upper limit for the relative radiance variations in the observed clouds was estimated from film density to be by a factor of between four and five. Variations of radiance were less for the smaller clouds. The radiance variations of the clouds gradually decreased as the diameter of the area viewed increased from 10 m to 800 m. Most radiance variations were resolved on the scale of 100 m with the radiometer.

ACKNOWLEDGEMENTS

The authors would like to thank Dr. Duane E. Stevens for his aid and guidiance, Mr. John T. Klehr for his help with the data collection and analysis, and Ms. Odilia Panella for her help in preparing the manuscript. Computer time was provided by the National Center for Atmospheric Research which is supported by the National Science Foundation.

TABLE OF CONTENTS

LIST OF FIGURES

LIST OF SYMBOLS

a	light source to screen distance
A_c	area projected onto a cloud side
a_e	equivalent radiometer sensor area
a_s	radiometer sensor area
A_s	cloud side area
A_T	cloud top area
d	radiometer to cloud side distance or distance measured on a slide
D	distance
H	cloud height
I_{tot}	total number of photons
I_{xi}	number of photons exiting the X face
I_{yi}	number of photons exiting the Y face
K	constant of proportionality
L	distance intercepted by the camera field of view
lwc	liquid water content
$\hat{n}$	unit vector normal to a cloud face
N	relative radiance
$P(\alpha)$	probability density function
$PP(\alpha)$	cumulative probability function
PR	probability
P_r	power recieved by the radiometer
P_{tot}	total power entering a cloud
r	droplet radius or correlation coefficient

R	aircraft to cloud center distance
RN	random number
s	geometric distance
$\hat{s}$	unit vector in the direction of a photon
V	radiometer voltage
V_o	zero power radiometer voltage
W	cloud width
X	x axis
X_a	aircraft x coordinate
X_c	cloud x coordinate
Y	y axis
Y_a	aircraft y coordinate
Y_c	cloud y coordinate
Z	z axis
α	scattering angle or radiometer field of view
α_s	solar azimuth angle
β	volume scattering coefficient
γ	second scattering angle
θ	zenith angle
θ_i	arbitrary zenith angle
θ_u	tilt of radiometer from horizontal
θ_o	solar zenith angle
λ	wavelength
τ	optical depth

LIST OF SYMBOLS continued

ϕ	azimuth angle
ϕ_i	arbitrary azimuth angle
ϕ_n	angle between normal to cloud face and radiometer viewing direction
ϕ_s	azimuth angle between incident solar direction and aircraft to cloud center line
ψ	azimuth angle between south and aircraft to cloud center line
ω	solid angle
$\bar{\omega}_o$	single scatter albedo

1.0 INTRODUCTION

An understanding of the radiative properties of clouds is essential for determing their effect on incoming solar radiation and in the interpretation of satellite observations. There has been extensive theoretical development treating clouds as semi-infinite plane parallel layers which has been summarized by Lenoble (1977). Initial efforts to treat finite clouds have been reported by Busygin, et al. (1973), McKee and Cox (1974, 1976), Davies and Weinman (1976), Barkstrom and Arduine (1976), Avaste and Vainikko (1976), and Davies (1978). Other aspects such as cloud inhomogeneities and absorption of radiation have been dealt with theoretically. McKee and Klehr (1978) studied the effect of a cloud turret and Wendling (1976) investigated clouds with periodic striations. Twomey (1976) reported theoretical calculations of absorption by both cloud droplets and water vapor for plane parallel clouds. Davis, et al. (1978) and Klehr and McKee (1978) made calculations of absorption by cloud droplets for finite clouds. The above results showed that finite cloud geometry, cloud inhomogeneities, and absorption can each have an effect on the radiative properties of clouds. There have also been a number of observational studies of cloud radiative properties such as Griffith and Woodley (1973) which correlated cloud top brightness with cloud height and Reynolds, McKee and Danielson (1978) which looked at the relation between cloud brightness and cloud size and microphysical properties.

The purpose of this study was to test the validity of a theoretical model. The data in this study were scans of the sides of moderate sized cumulus clouds taken from an aircraft with a visible radiometer. The theoretical model used the Monte Carlo technique of radiative transfer for a finite water cloud. The model considered a homogeneous right parallelepiped (slab cloud) and absorption was neglected. Model and observed results were compared to verify the theoretical model and to determine the limitations of this simplified model of a cloud.

2.0 DATA DESCRIPTION

The data set for this study was collected during four days in the summer of 1977 over the plains of eastern Colorado. The NCAR research aviation facility Queen Air equipped with a side looking visible radiometer and a data recording system was flown around moderate sized cumulus clouds (1-3 km thick). Vertical scans of the cloud sides were taken at various positions around each cloud. The radiometer was equipped with an optically aligned camera, and a photograph was taken just before each radiometer scan.

2.1 Description of the radiometer

The radiometer used consisted of three parts: a passive black tube which restricted the field of view, a photomultiplier tube which converted incident power to voltage and a voltage amplifier. The radiometer was designed so that the output voltage would be linear with incident power. This relationship was checked by pointing the radiometer at a translucent screen illuminated from behind by a nondirected light source. The radiometer to screen distance was fixed while the light source to screen distance was varied. The power received by the radiometer is proportional to $1/a^2$ where a is the light source to screen distance. Figure 1 is a graph of radiometer output voltage versus $1/a^2$. A voltage reading of +4.9 volts corresponds to darkness and a bright cloud reading was about -1.5 volts. As can be seen from figure 1, the output voltage (V) is approximately linear with incident power (P_r) over the range of values in the data and can be written as:

$$P_r = K(V_o - V) = K \Delta V \qquad (2.1)$$

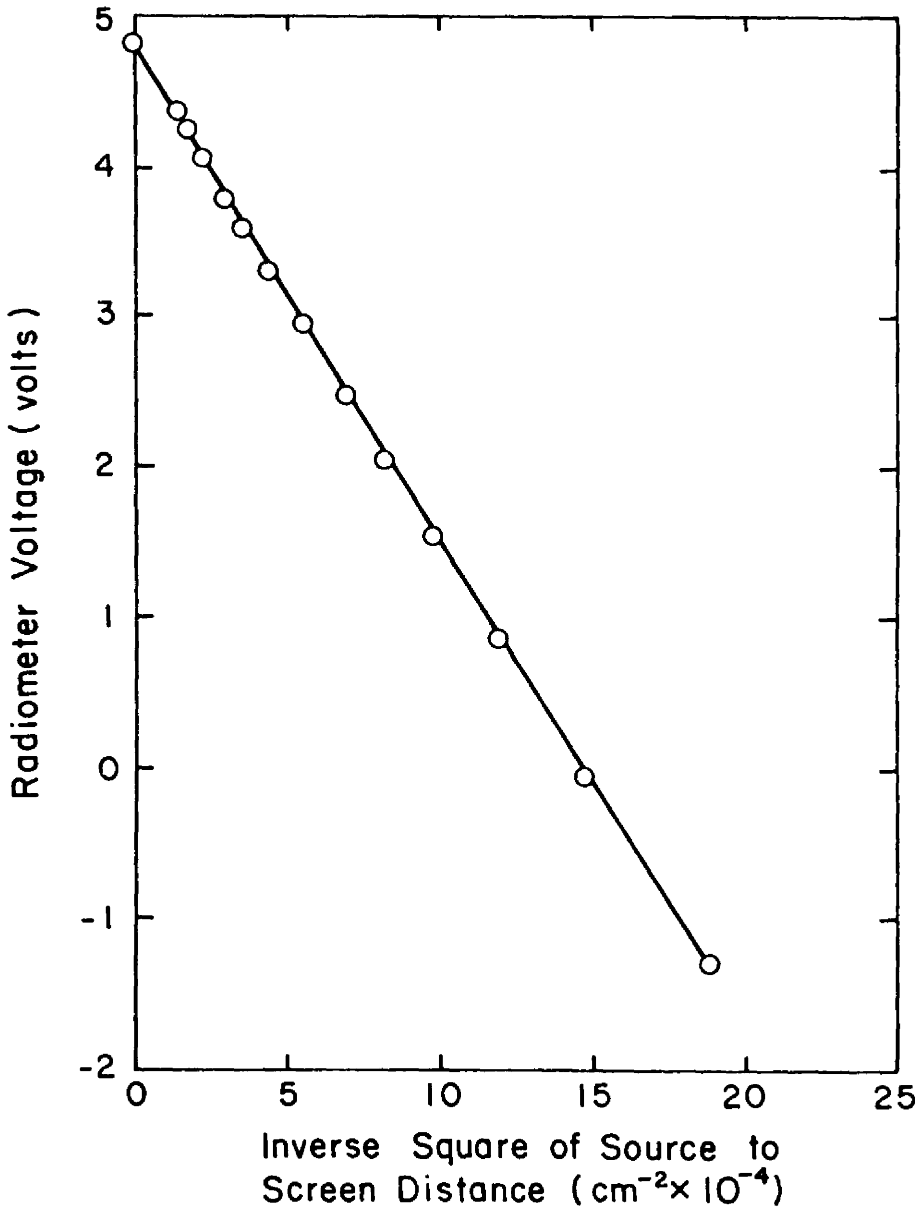

Figure 1. Radiometer voltage versus inverse square of source to screen distance.

where K is some constant and V_0 is the voltage reading which corresponds to zero power. All the comparisons in this study are relative so no absolute calibration of the radiometer was made. Results will be presented in terms of ΔV which is directly proportional to power. For reference, when the radiometer viewed a sheet of white paper exposed to direct sunlight, ΔV was 7.3 volts. The brightest cloud in the data had a ΔV of 6.4 volts.

The field of view of the radiometer was determined by moving a small light source inside the field of view until ΔV of the radiometer was maximized. The source was then moved small distances perpendicular to the line from the radiometer to original source position. Knowing the radiometer to source distance, each small displacement corresponded to an angular field. Figure 2 shows the map of the radiometer field of view where the radiometer was oriented in the same way as on the aircraft. The ratio of ΔV to the maximum value of ΔV (ΔV_{max}) is plotted versus angular displacement from the original position. The ratio of ΔV to ΔV_{max} goes to zero at an angular displacement of about one degree in all directions from the original source position, with a half power point at about 0.6 degrees. The total field of view of the radiometer is then about 2 degrees with a half power point at about 1.2 degrees.

The detector of the radiometer was sensitive to radiation with wavelengths less than about 1 μm. A red filter was used which was sensitive to wavelengths greater than about 0.6 μm. Figure 3 shows the resultant sensitivity of the detector and the filter. The radiometer is sensitive to a small wavelength interval centered about 0.8 μm with a half width of about 0.3 μm.

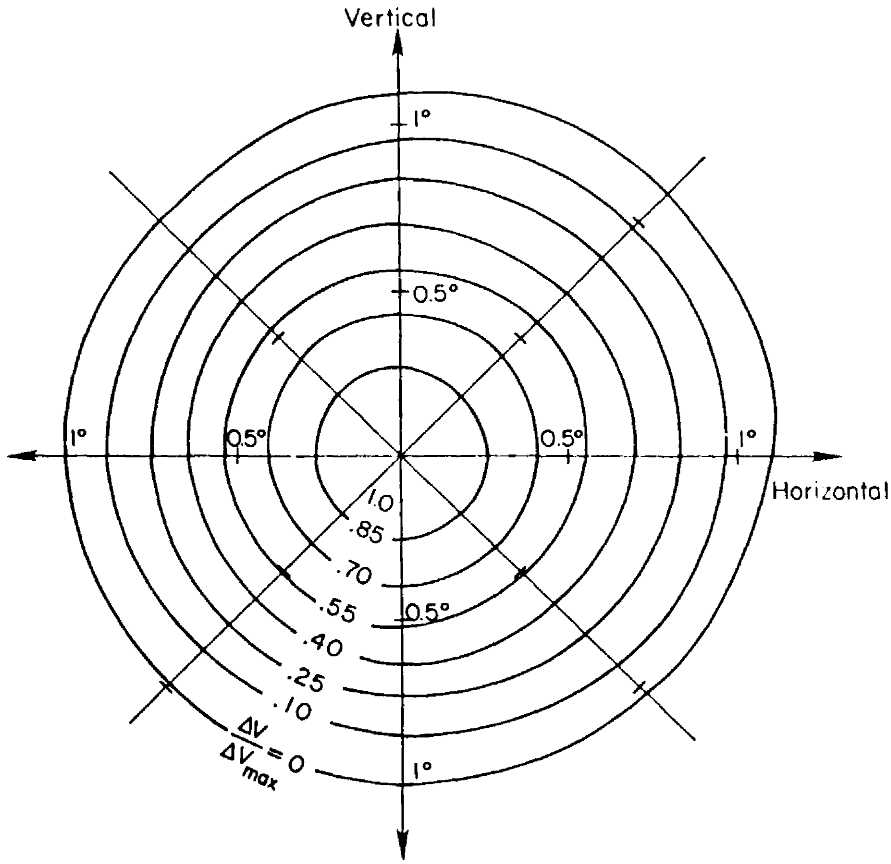

Figure 2. Field of view of the radiometer.

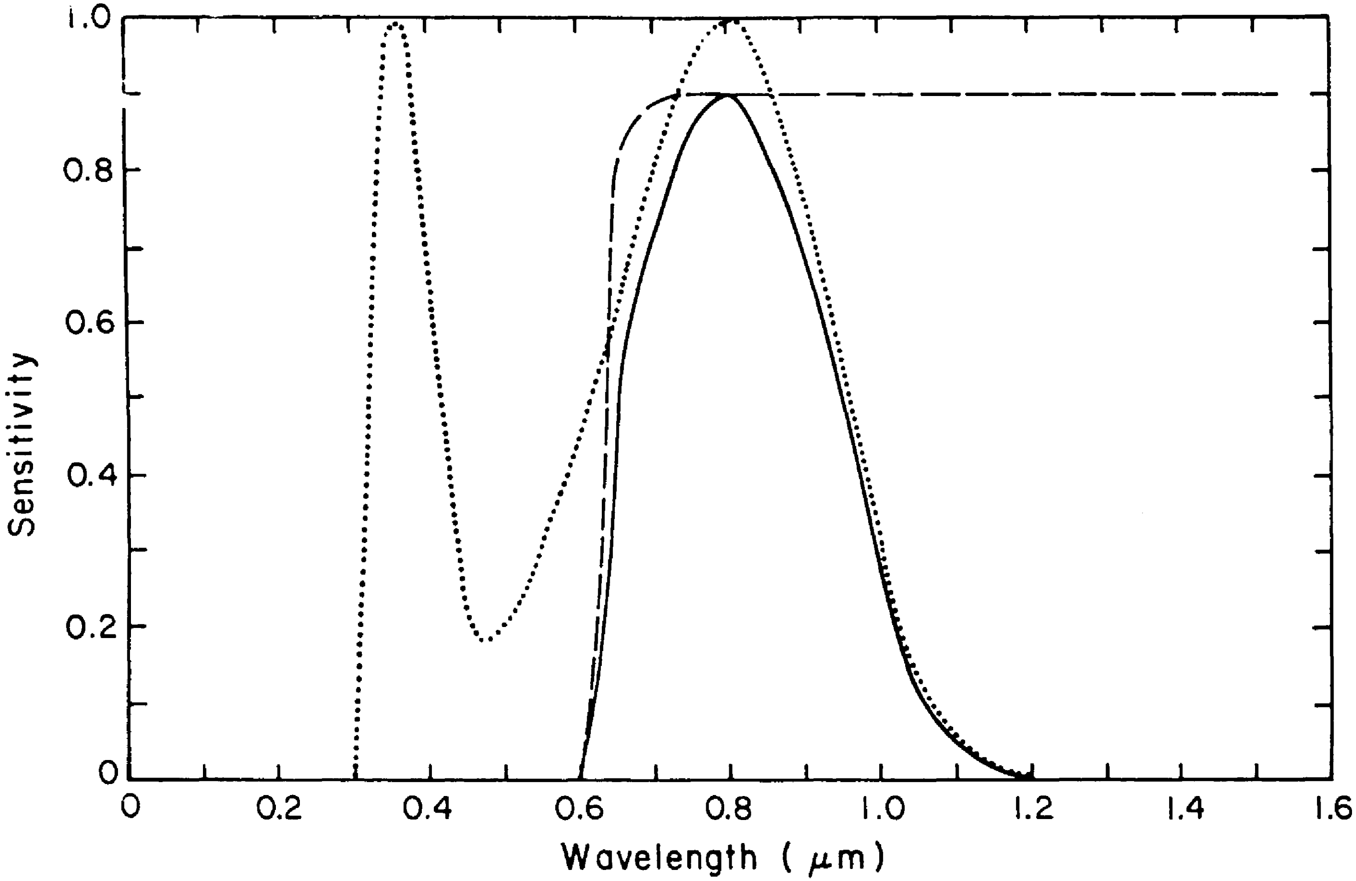

Figure 3. Sensitivity versus wavelength (Filter (dashed), detector (dotted), filter and detector (solid)).

2.2 Data collection

The NCAR Queen Air was equipped with an inertial navigation system and a data recording system. Thirty-three parameters were stored on nine track tape at various rates. The parameters relevant to this study and their respective storage rates are listed in Table 1.

Table 1. Relevant parameters and storage rates

Parameter	Storage rate (number per second)
Radiometer voltage	8
Aircraft latitude	1
Aircraft longitude	1
Aircraft heading	1
Horizontal wind velocity	1
Liquid water content	1
Ambient temperature	1

The optically aligned camera was modified so that the time to the nearest second was printed on each photographic slide. The slides were then used to identify the time of each scan. The camera and radiometer were mounted on the left side of the aircraft and counterclockwise circles were flown around each cloud at various levels between cloud base and the cloud top. The radiometer was operated manually, and each of the scans was taken in the same way. First, the radiometer was aimed at about the center of the cloud and a picture was taken. An upward vertical scan was taken until the radiometer field of view left the top of the cloud, followed by a downward scan from cloud top to cloud base. The upward scans lasted about 4 seconds and from 4 to 13 scans were taken of each cloud.

The aircraft was flown on four days, and several clouds were studied on each day. All the second day's data were lost due to a bad data tape, so three days of data were obtained. The original intent of the experiment was to fly around, over and through small cumulus clouds. The radius of the circle flown around each cloud was about 5 kilometers and the groundspeed of the Queen Air was about 80 m/sec. The time to fly around a cloud was then about six minutes. During this time some clouds would undergo large changes, and at times would completely dissipate. For this reason, scans of the cloud sides only were taken. Scans of nine clouds were obtained and five of these were chosen for study on the basis of the number of scans per cloud and on how much the clouds changed between scans. Before the analysis of the data for each cloud is discussed, a description of the numerical model is given.

3.0 MONTE CARLO MODEL

The Monte Carlo method has been described in detail in Cashwell and Everett (1959) and has been applied to a number of radiative transfer problems. Kattawar and Plass (1971) and Danielson, et al. (1969) have used the Monte Carlo method in semi-infinite cloud layer scattering computations. Busygin, et al. (1973) and McKee and Cox (1974, 1976) have used the Monte Carlo method for finite shaped clouds. The model used in this study is a version of the model described in McKee and Cox (1974, 1976) and McKee and Klehr (1978). The following description is based on McKee and Cox (1974). Justification of the various assumptions in the model will be discussed in chapter 5.

The Monte Carlo method essentially is a direct simulation of the radiative processes inside a cloud. A cloud is defined by a set of boundaries and a photon enters the cloud from a specified direction. The distance to a scatter is determined and a new direction of travel is chosen from an appropriate phase function. The above process is repeated until the photon escapes through a boundary. (A more general form of the model includes droplet absorption which was neglected for reasons to be discussed in chapter 5). The distance between interactions and the phase function depend on specified microphysical properties and on the wavelength of the interacting radiation.

The present model considers an isolated cloud with no surrounding atmosphere or ground reflection. The cloud is assumed to be homogeneous and composed of water droplets with a size distribution given by

$$n(r) = 2.373\ r^{6} \exp(-1.5r) \tag{3.1}$$

where r is the droplet radius in microns and n(r) is the number of droplets cm^{-3} μm^{-1}. This distribution was taken from Diermendjian (1969) and is referred to as a C1 distribution which is a model for a cumulus cloud. For 100 droplets cm^{-3}, the above distribution results in a liquid water content of 0.063 $g\,m^{-3}$. The volume scattering coefficient (β) depends on the wavelength of the interacting radiation, the droplet distribution, and the amount of scattering material per unit volume (liquid water content). For a wavelength of 0.7 μm and the C1 distribution, β is given by

$$\beta = \left(\frac{lwc}{.063}\right) 16.73 \text{ km}^{-1} \tag{3.2}$$

where lwc is liquid water content expressed in $g\,m^{-3}$. Since the cloud is assumed to be homogeneous, optical depth (τ) is related linearly to geometric distance (s), given by

$$\tau = \int_0^s \beta ds \tag{3.3}$$

A 1.5 km thick cloud with a liquid water content of 0.15 $g\,m^{-3}$ will have an optical depth of 60.

The distance a photon travels between interactions is simulated by interpreting the fraction of the incident radiation transmitted through a given distance ($e^{-\tau}$) as the probability that a photon will travel through that same distance without an interaction (PR). That is;

$$e^{-\tau} = \exp\left(-\int_0^s \beta ds\right) = PR \tag{3.4}$$

A random number between zero and one (RN) is chosen for PR, and the distance to the next interaction (s) is determined by solving for the upper limit of integration of

$$\int_0^s \beta ds = \tau = -\ell n(RN) \tag{3.5}$$

The single scattering phase function $P(\alpha)$ defines the angular distribution of the radiation after a scattering event. The angle α is measured from the direction of propagation before the scatter to the direction after the scatter. The phase function $P(\alpha)$ is shown in figure 4 for the C1 distribution at a wavelength (λ) of 0.7 μm. The phase function is characterized by a strong forward scattering peak. The phase function is normalized so that the integral over all solid angles equals one. That is;

$$\iint_\omega P(\alpha)\ d\omega = \int_0^{2\pi}\int_0^{\pi} P(\alpha)\ \sin\alpha\, d\alpha\ d\gamma = 1 \tag{3.6}$$

where ω is solid angle and γ is the angle of rotation about the original direction of propagation. The phase function is independent of γ so that

$$2\pi\int_0^{\pi} P(\alpha)\ \sin\alpha\, d\alpha = 1 \tag{3.7}$$

The probability that a photon will be scattered between 0 and α ($PP(\alpha)$) is then

$$PP(\alpha) = 2\pi\int_0^{\alpha} P(\alpha')\ \sin\alpha'\ d\alpha' \tag{3.8}$$

The probability density function $PP(\alpha)$ is shown in figure 5. There is a 50% probability that a photon will be scattered between 0° and 10°, which reflects the strong forward scattering peak. A random number between zero and one is chosen for $PP(\alpha)$ and the upper limit of integration in (3.8) is solved for, which is the scattering angle α. The

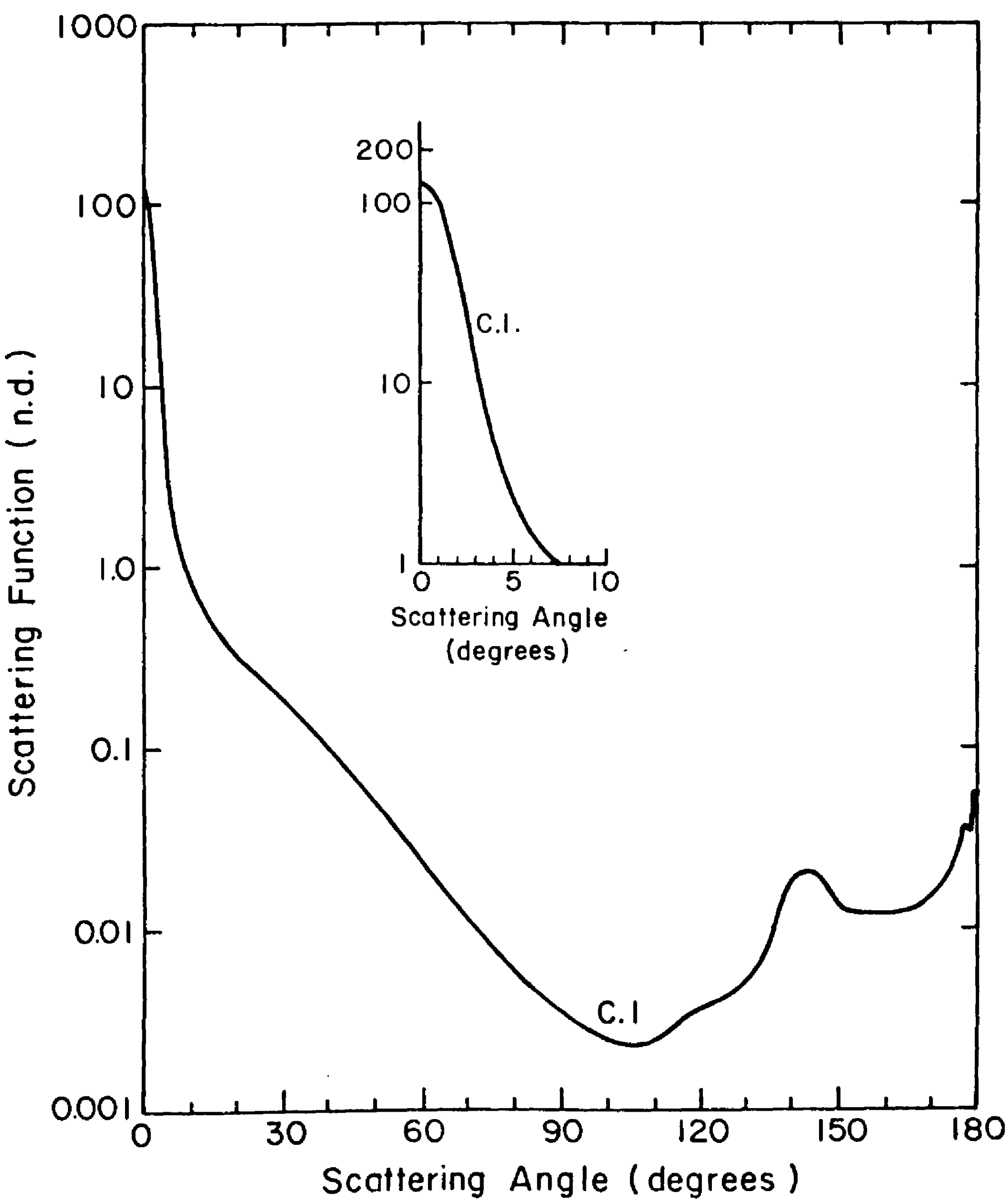

Figure 4. Scattering phase function for C1 model at $\lambda = 0.7\ \mu m$.

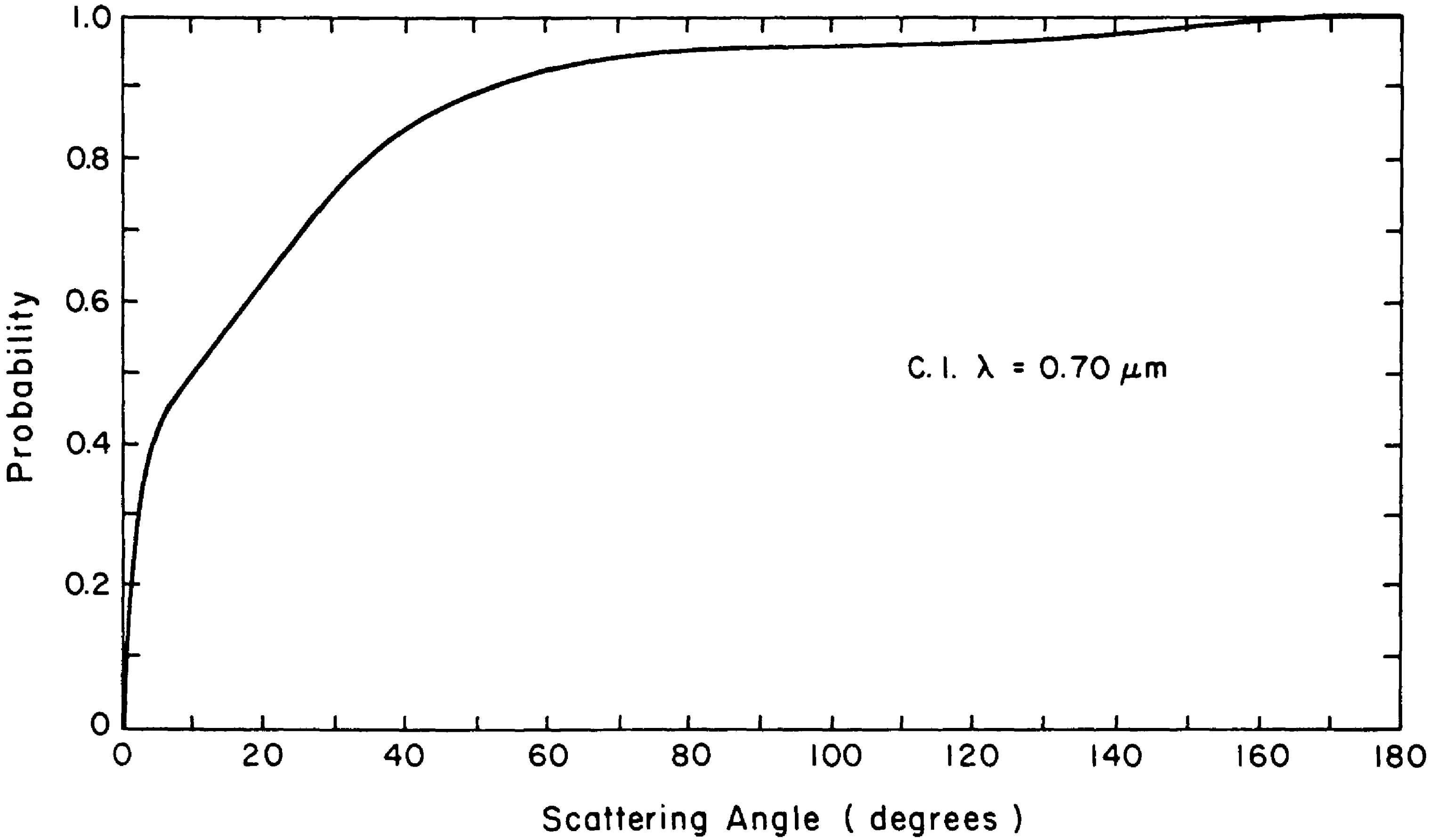

Figure 5. Cumulative probability density function for Cl model at $\lambda = 0.7$ μm.

second angle γ is chosen randomly between 0 and 2π. These two angles specify the new direction of travel.

The cloud geometry used in the model is a right parallelepiped (slab cloud). Figure 6 shows the slab cloud and the coordinate system used. The incident solar beam is plane parallel and is always in the Y-Z plane. This restricts direct sunlight to the slab top and the +Y face. Photons randomly enter the top and +Y side of the slab in proportion to the incident solar angle and the cloud top and side areas. For example, suppose that I_{tot} photons enter a slab with a cloud top area of A_T and a +Y side area of A_s from a zenith angle of θ_o. Then $I_{tot}A_T \cos\theta_o \,/\, (A_T \cos\theta_o + A_s \sin\theta_o)$ photons enter the top and $I_{tot}A_s \sin\theta_o \,/\, (A_T \cos\theta_o + A_s \sin\theta_o)$ enter the +Y side. In the model, the X and Y dimensions of the cloud are equal so that the areas of X and Y faces are equal. When a photon exits the cloud, its direction of travel is specified by the zenith angle θ measured from the +Z axis and an azimuth angle ϕ measured from the -Y axis. A ϕ value of 0 is opposite the sun and a ϕ value of π is towards the sun.

The model output gives radiance values for each of the slab faces averaged over a finite solid angle $\Delta\omega$, where

$$\Delta\omega = \Delta(\cos\theta)\,\Delta\phi \tag{3.9}$$

for $\Delta(\cos\theta)=0.05$ and $\Delta\phi = \pi/12$. All radiances are relative to an incident solar irradiance of π. The following is an example of how a radiance value is calculated. Suppose again that I_{tot} photons enter a slab cloud with a top area of A_T and side area of A_s from the direction specified by the zenith angle θ_o. Suppose that I_{xi} of these photons exit the +X face into some solid angle defined by the azimuth

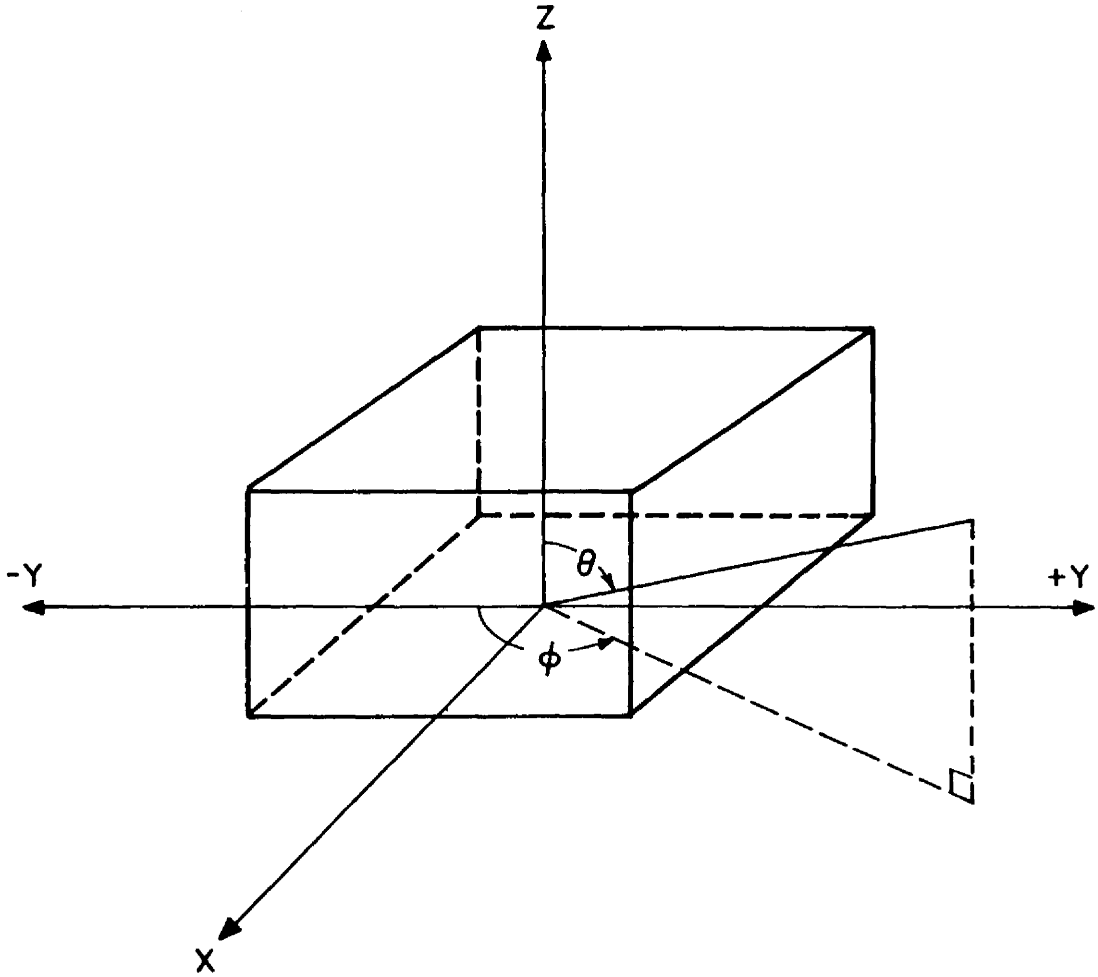

Figure 6. Slab cloud with coordinate system.

angles ϕ_i and $(\phi_i + \pi/12)$ and the zenith angles specified by $\cos\theta_i$ and $(\cos\theta_i + .05)$. Since the solar irradiance is taken to have a value of π, the total power entering the slab (P_{tot}) is given by

$$P_{tot} = (\pi A_T \cos\theta_o + \pi A_s \sin\theta_o) \qquad (3.10)$$

The total number of photons entering the cloud (I_{tot}) is equivalent to the amount of power P_{tot} so that the power per photon is equal to P_{tot} / I_{tot}. Then the power represented by I_{xi} photons is

$$I_{xi} \left(\frac{P_{tot}}{I_{tot}}\right) = \frac{I_{xi}}{I_{tot}} \pi (A_T \cos\theta_o + A_s \sin\theta_o) \quad . \qquad (3.11)$$

Radiance (N) is defined as the power per unit area and solid angle which passes perpendicular to that area. The model radiances are for a wavelength of 0.7 μm and are given by

$$N = \frac{\text{Power}}{\Delta\omega \;\; \Delta A \, (\hat{n} \cdot \hat{s})} \qquad (3.12)$$

where $\Delta\omega$ is the finite solid angle, ΔA is the area of a slab face, $\hat{n}$ is the unit vector perpendicular to the slab face and $\hat{s}$ is the unit vector in the direction of the exiting photons. In this example ΔA is the area of the +X face (A_s) and $\Delta\omega$ is given by equation (3.9). The dot product of $\hat{n}$ and $\hat{s}$ is approximated by

$$\hat{n} \cdot \hat{s} \cong \overline{\sin\theta_i} \;\; \overline{\sin\phi_i} \qquad (+X \text{ face})$$

$$\hat{n} \cdot \hat{s} \cong \overline{\sin\theta_i} \;\; \overline{\cos\phi_i} \qquad (+Y \text{ face}) \qquad (3.14)$$

where $\overline{\sin\phi_i}$ and $\overline{\cos\phi_i}$ are the averages of the sine and cosine of the azimuth angles ϕ_i and $(\phi_i + \pi/12)$ and $\overline{\sin\theta_i}$ is the average sine of the zenith angles specified by $\cos\theta_i$ and $(\cos\theta_i + .05)$. The power is given by equation (3.11) and the radiances for the +X face are then

$$N_{xi} = \frac{I_{xi}}{I_{tot}} \left[\frac{\pi (A_T \cos\theta_o + A_s \sin\theta_o)}{(\pi/12)\ (.05)\ (A_s)\ (\overline{\sin\theta_i}\ \overline{\sin\theta_i})} \right]$$

or

$$N_{xi} = \frac{I_{xi}}{I_{tot}} \left[\frac{\left(\frac{A_T}{A_s}\right) \cos\theta_o + \sin\theta_o}{(.05/12)\ (\overline{\sin\theta_i}\ \overline{\sin\phi_i})} \right] \tag{3.14}$$

For the +Y face the radiances are given by

$$N_{yi} = \frac{I_{yi}}{I_{tot}} \left[\frac{\left(\frac{A_T}{A_s}\right) \cos\theta_o + \sin\theta_o}{(.05/12)\ (\overline{\sin\theta_i}\ |\ \overline{\cos\phi_i}\ |\ )} \right] \tag{3.15}$$

where I_{yi} is analogous to I_{xi}. Equations (3.14) and (3.15) also apply to the -X and -Y faces respectively. The model keeps track of how many photons exited each face into each of the solid angle boxes and computes the radiances from the above formulas.

The value of I_{tot} is usually specified to be 20,000 photons. The photons enter the cloud in groups of 2,000 , and statistical analyses of these groups give an indication of the random noise in a particular model run.

4.0 DATA ANALYSIS

As described in chapter 2, five clouds were chosen for study, and several vertical scans were taken of the sides of each of these clouds. The position of the cloud at the time each scan was taken is estimated. The relative radiometer, solar and cloud orientation is then determined. The height and width of each cloud are estimated from photographs, and the interpretation of the radiometer scans is discussed.

4.1 Estimation of cloud position

First, the aircraft position and heading were plotted on a horizontal grid for each of the times a picture was taken. The latitude and longitude of the aircraft were converted to distances north and east of the take off point. This plot for cloud 1 is shown in figure 7 as an example. The arrow at each of the outer points is the aircraft heading. The optically aligned camera was pointed approximately 90° to the left from the front of the aircraft and could be moved 15° to either side in the azimuthal direction to allow the cloud to be sighted, and was not restricted in elevation to allow vertical scans. Originally potentiometers were attached to the radiometer so that the azimuth and elevation angles would be known. These potentiometers malfunctioned so that no information of the elevation angle was obtained and azimuth information was available only for clouds 1 and 2. Even this information is of limited value since the azimuth potentiometer malfunctioned in such a way that it could not be calibrated. The sign of the output voltage does determine whether the radiometer was pointed to the left or right of center. Some information on the azimuth

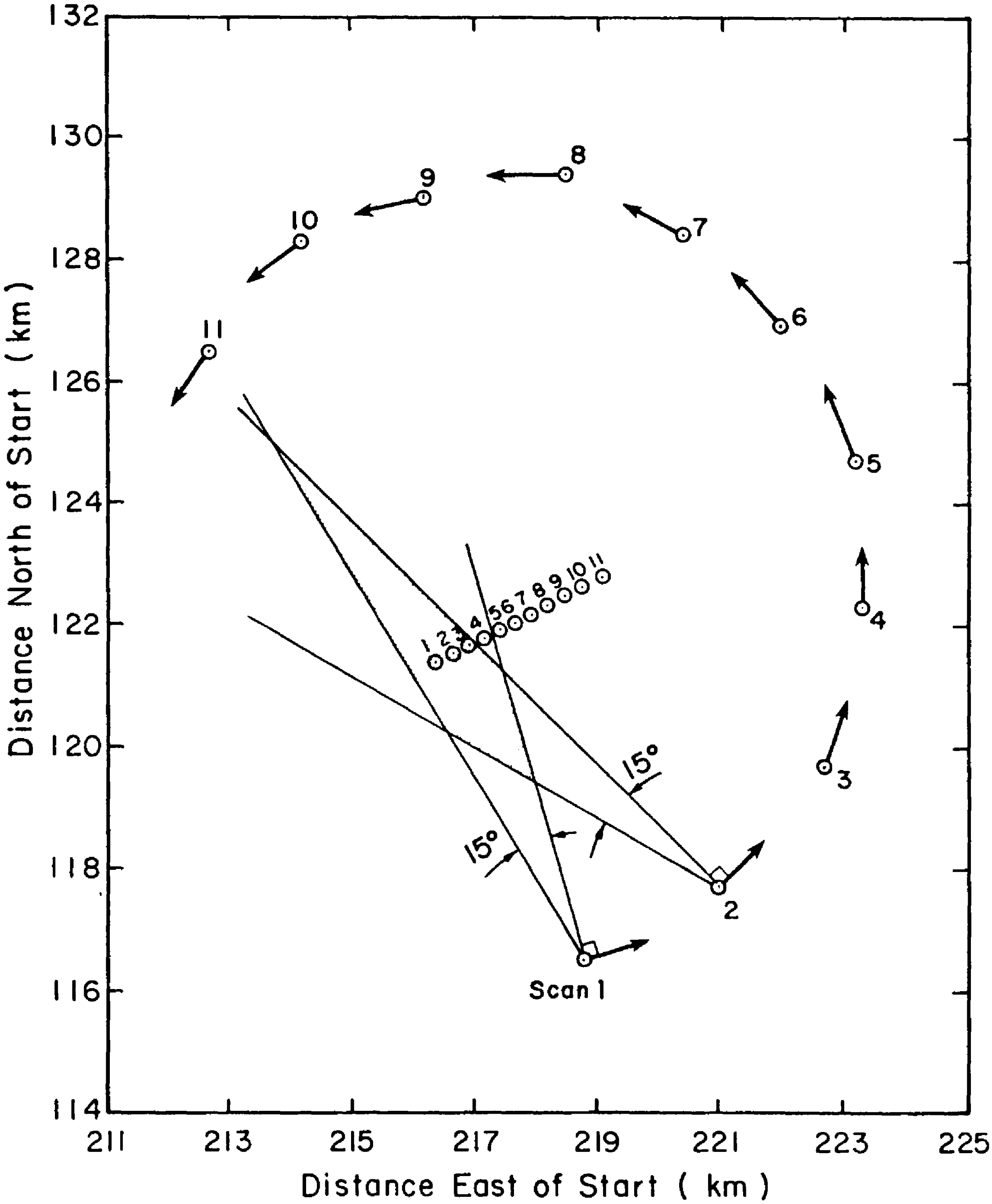

Figure 7. Aircraft positions and estimated cloud positions for cloud 1.

position was inferred from the slides. If the radiometer was pointed to the right of center, a part of the aircraft wing showed up in the slide. Using this and the sign of the potentiometer voltage, it was determined whether the radiometer pointed to the left or right of center. This defined the azimuth angle of the radiometer and camera to within 15° of where it pointed when each picture was taken. An average value for the horizontal wind was determined from positions around the cloud. Using the average wind as a guide, the direction the cloud moved and the distance the cloud moved between scans was estimated. The position of the cloud center at each of the scan times was then estimated by an iterative process. The position of the cloud center at the time of the first scan was estimated by seeing where the two lines drawn 90° to the left of the first two aircraft headings intersected. This position was adjusted to take into account whether the radiometer was pointed to the left or right of center. In figure 7, the shaded area shows the region where the first cloud center position could be. Once the position of the cloud at the first slide time was estimated, the cloud positions at the other slide times were plotted based on the average wind. These positions were checked to see if they were in the 15° range of where the radiometer was pointing from the other aircraft positions. If the computed points were not in this range, the first point was adjusted and the above process was repeated. This was done until all the computed points were in the 15° range of all the aircraft positions. The points in the center of figure 7 are the estimated positions of the center of cloud 1 when each of the vertical scans were taken. To get a rough idea of the accuracy of the estimated cloud positions, the position of the cloud at the time of the first scan in figure 7 can be moved about ½ km in any direction with the rest of the positions remaining in the 15° range of the other aircraft positions.

4.2 Solar, cloud and radiometer orientation

After the cloud center positions were estimated at the time of each scan, the average latitude and longitude of the cloud was found from the horizontal grid. Using this, the time of each scan, and the day of the year, the solar azimuth and zenith angles were computed from the well known sun angle formulas. The solar azimuth is measured eastward from south, and the zenith angle is measured from the local vertical. Using the solar azimuth angle and the horizontal coordinates of the aircraft (X_a, Y_a) and the cloud center (X_c, Y_c) from the grid, the azimuthal angle between the line from the sun to the cloud and the line from the cloud center to the aircraft was determined (ϕ_s). Figure 8 shows how this is measured. The angle ψ is measured from the southward direction counterclockwise to the line from the cloud center to the aircraft position. As can be seen from figure 8;

$$\cos\psi = \frac{(Y_c - Y_a)}{\sqrt{(Y_c - Y_a)^2 + (X_c - X_a)^2}}$$

$$\psi = \cos^{-1}\left[\frac{(Y_c - Y_a)}{\sqrt{(Y_c - Y_a)^2 + (X_c - X_a)^2}}\right] \qquad (4.1)$$

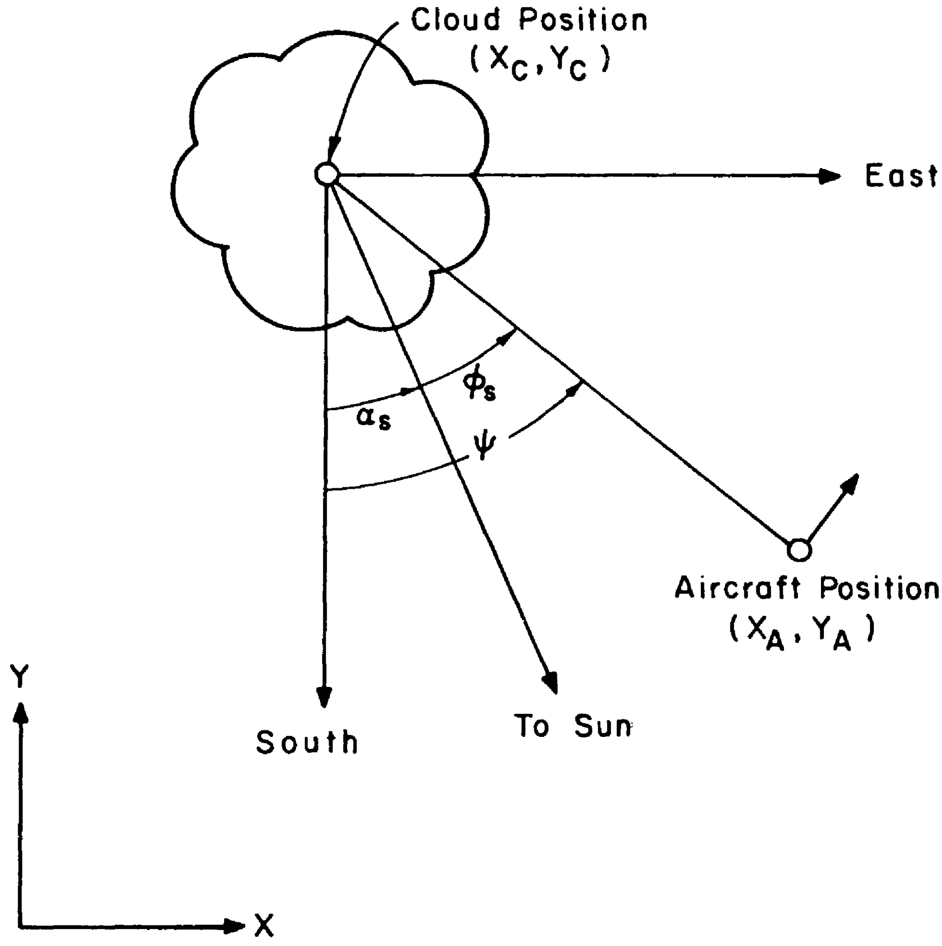

Figure 8. Determination of solar, cloud and aircraft orientation.

The angle ϕ_s is then

$$\phi_s = (\psi - \alpha_s) = \cos^{-1}\left[\frac{(Y_c - Y_a)}{\sqrt{(Y_c - Y_a)^2 + (X_c - X_a)^2}}\right] - \alpha_s \qquad (4.2)$$

where α_s is the solar azimuth angle. In this particular coordinate system, when X_a is less than X_c, ϕ_s is given by

$$\phi_s = (-\psi - \alpha_s) \qquad (4.3)$$

Using (4.2) or (4.3), the angle ϕ_s was computed for each scan. This angle is a measure of where the radiometer is pointed in relation to the horizontal projection of the sun's rays at the time of each scan. A ϕ_s value of zero would indicate that the radiometer was pointed at the side of the cloud the sun was striking and a ϕ_s value of π would be on the antisolar side of the cloud. This is opposite to the way ϕ is defined in the model. In all the model and data comparisons, the above definition of ϕ_s will be used.

Each radiometer scan lasted about four seconds, so that ϕ_s was actually changing during each scan. The groundspeed of the Queen Air was about 80 m/sec and the cloud center to aircraft distance was about 5 km, so ϕ_s changes by less than 4 degrees in 4 seconds. Since the Monte Carlo model radiances are averaged over 15 degrees of azimuth angle, the variation of ϕ_s during each scan was not taken into account.

4.3 Estimation of cloud dimensions

Using the horizontal coordinates of the aircraft position and cloud center at the time of each scan, the aircraft to cloud distance was calculated. Using this, estimates of the cloud dimensions can be made from measurements off the slides. The slide dimensions are 36 mm by 24 mm and the field of view of the camera is 46° . In figure 9, a camera is aimed at the center of a cloud, a distance R away. The distance that is intercepted by a 46° field of view at a perpendicular distance R corresponds to 36 mm on the slide. This is the distance L in figure 9 and is given by

$$L = 2R \tan 23° \qquad (4.4)$$

Since the distance L corresponds to 36 mm on the slide, the conversion from distance measured off the slide (d) to actual distance D is given by

$$D = d\left[\frac{2R \tan 23°}{36 \text{ mm}}\right] \qquad (4.5)$$

where d is measured in millimeters. Using (4.5), estimates of cloud widths and heights were made for each scan, where the cloud center to aircraft distance was used for R .

4.4 Interpretation of the radiometer scans

As described earlier, the radiometer scans consisted of an upward scan off the cloud top followed by a downward scan to the ground. Since the radiometer used a red filter, the time when the field of view left the cloud onto blue sky was easily identified by a rapid decrease in ΔV . Assuming that the scan began just after each slide was taken, the beginning and end of the upward scans were found. The beginning of the downward scan was easily identified by a rapid increase in ΔV , but the time when the radiometer field of view left the bottom of the cloud was difficult to determine. For this reason, only the upward scans were used.

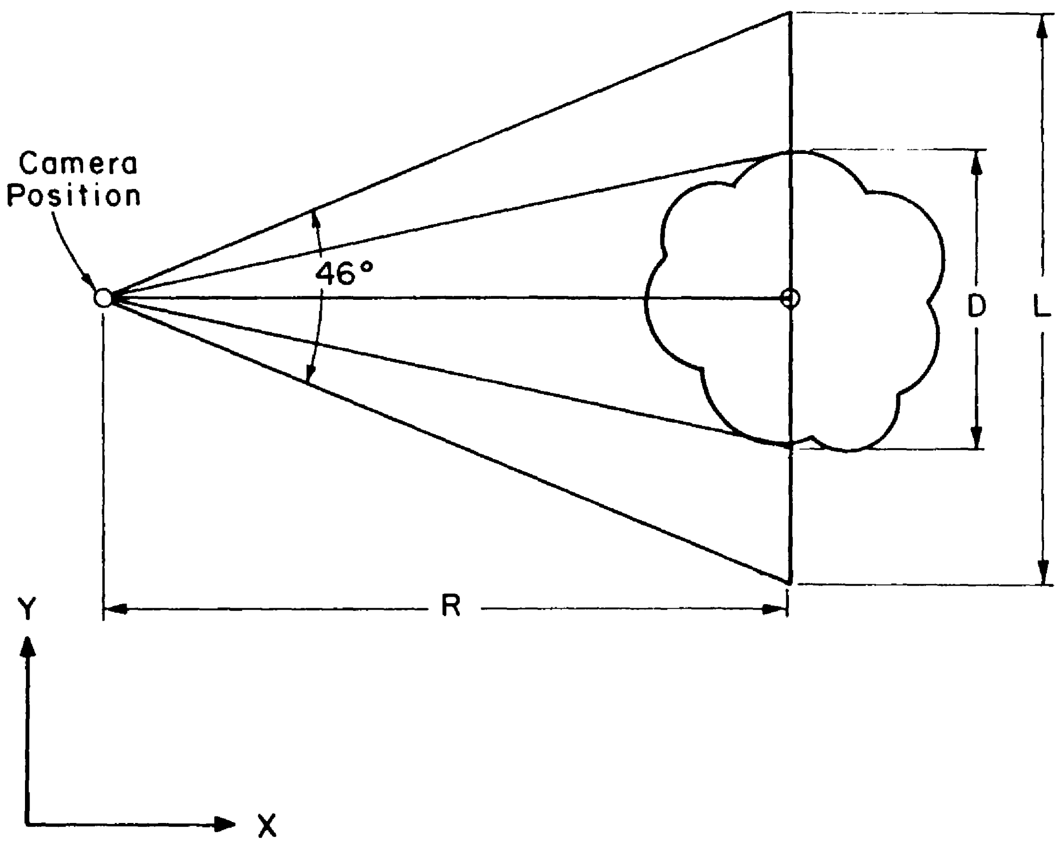

Figure 9. Estimation of cloud dimensions from photographs.

Since the radiometer and camera were optically aligned, it was possible to determine the point on the cloud where each scan began. The total field of view of the radiometer was 2° with a half power point at 1.2° . Most of the power received by the radiometer was within a field of view of 1.2° . The cloud to aircraft distance was about 5 km, so that each point of the radiometer scan represented an average over a circular area with a diameter of about 100 meters. The average height of the clouds was about 2 km so the diameter of the circle was about 1/20 of the cloud height. This spot was small enough so that many of the small scale cloud features could be resolved and showed up as maxima or minima in the radiometer scans.

Figure 10 shows the first five scans of cloud 1. The ordinate is ΔV which is proportional to power and the abscissa is time. These scans begin just below the center of the cloud and end at the cloud top. The cloud top was identified by a rapid decrease in ΔV (where the scan plot becomes dashed in figure 10). When the scan reached the top of the cloud, ΔV decreased to less than 0.5 volts (not shown in figure 10). This distinguished the cloud top from dark areas on the cloud where ΔV did not go below about 1.0 volts. The effects of small scale cloud features can be seen.

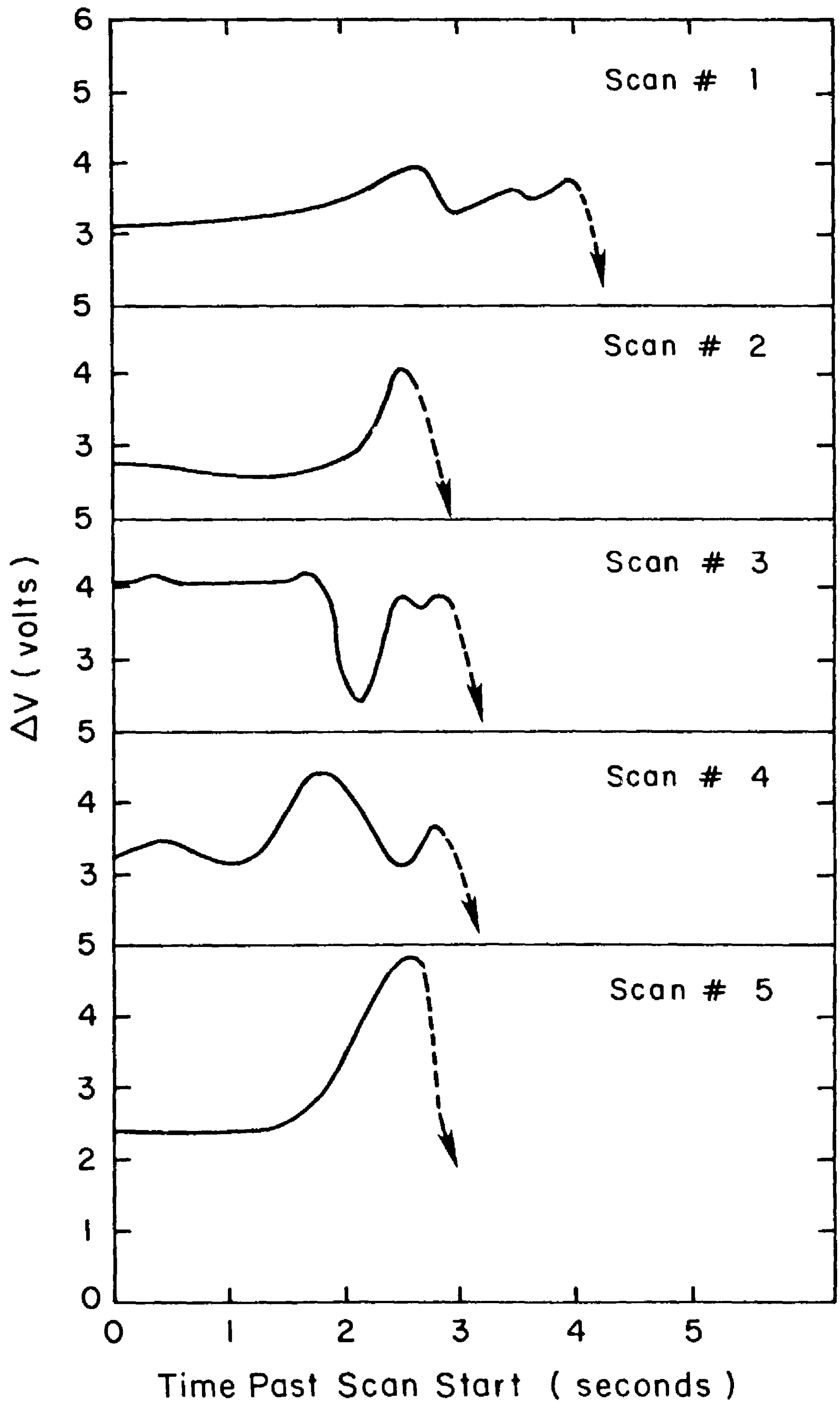

Figure 10. The first five radiometer scans of cloud 1.

5.0 MODEL AND DATA COMPARISONS

As described in chapter 3, the model requires a number of input parameters. The cloud droplet distribution, liquid water content and wavelength of the interacting radiation determine the phase function and volume scattering coefficient. The model results also depend on the geometric cloud dimensions and the solar zenith angle. Before model results and actual data are presented, each of these parameters is discussed.

5.1 Estimation of model input parameters

The five clouds in this study were non-precipitating continental cumulus with vertical depths ranging from about one to three kilometers. The clouds had the appearance of being composed of liquid water only. The ambient temperature at various levels around the clouds was no colder than about -5° C which is too warm for appreciable ice nucleation. One of the shortcomings of the data set is that no droplet size distribution information was collected. Auer (1967) studied the microphysical properties of non-precipitating continental cumulus clouds. The data for his study were collected during the summer of 1966 over the plains of eastern Colorado which is the same region as this study. The average vertical height of the clouds in his study was about two kilometers which agrees well with the clouds in this study. Figure 11 shows the average droplet size distribution of 13 non-precipitating cumulus clouds from the study by Auer and the C1 droplet distribution from Diermendjian used in the Monte Carlo model. Both distributions shown are for a liquid water content of 0.15 gm^{-3}. The general shape

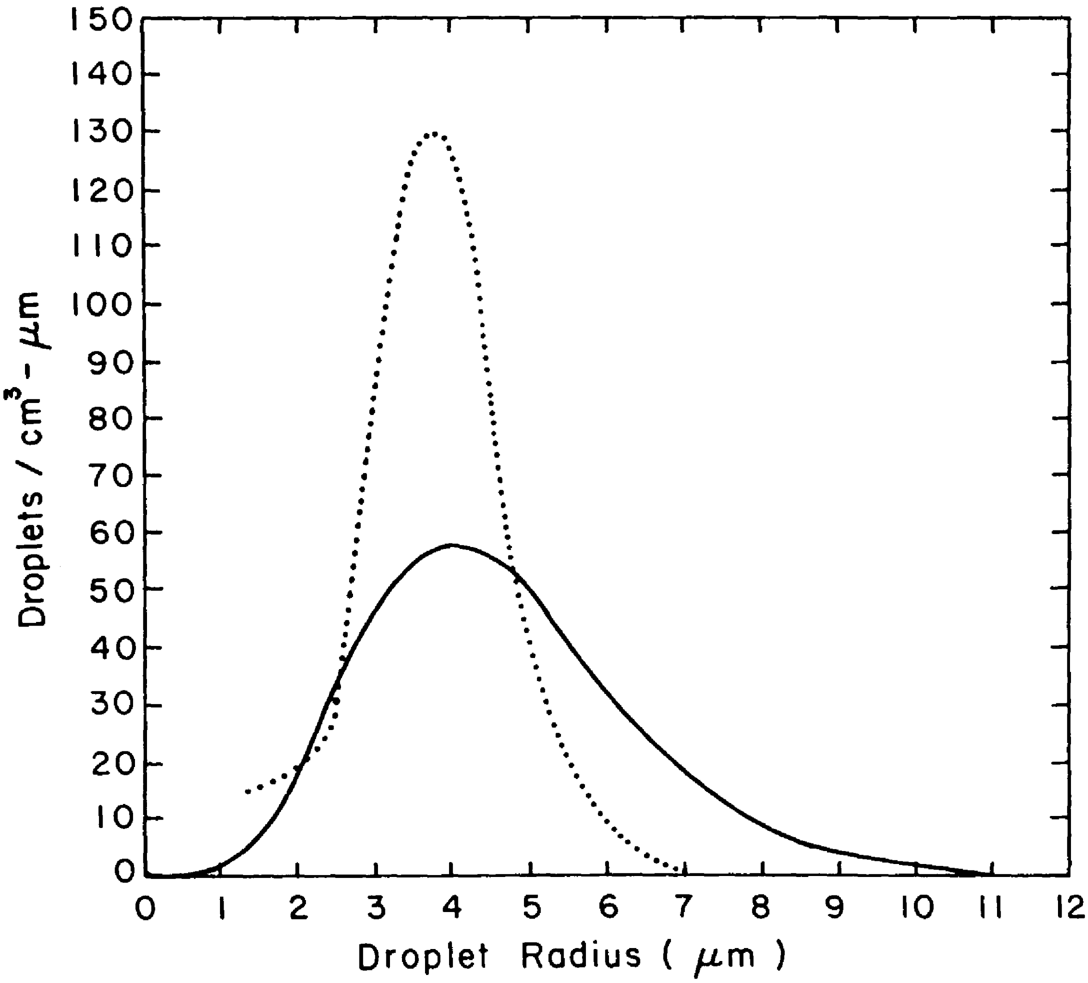

Figure 11. Droplet size distribution (Average observed distribution from Auer (dotted), C1 model (solid)).

of the two distributions is similar and neither contains many droplets with radii larger than about 10 μm. The mode droplet radius of both distributions is about 4 μm. The difference between the two distributions is that the C1 distribution contains a larger number of larger drops and has a wider shape. The measurements of droplet size distribution in the study by Auer were limited to the lower portion of the clouds. Warner (1969) studied the general features of the droplet spectrum of cumulus clouds. His results showed that the change in droplet concentration with height was not significant for most of the clouds studied, although there was some evidence that the droplet distribution becomes more skewed towards larger drops as the height above cloud base increases. McKee and Klehr (1978) compared results from a Monte Carlo model identical to the model described in chapter 3, using two different droplet distributions. Results using the C1 droplet distribution were compared to a much narrower distribution with a mode droplet radius of 2 μm (C3 distribution from Diermendjian). For a slab cloud with an optical depth of 60, the maximum difference between the radiance values was about 6%. The radiance values for the two distributions had the same shape as a function of solid angle. The C3 distribution is even narrower than the distribution from Auer and contains no droplets of radius greater than 4 μm. If the average distribution shown by Auer is assumed to be representative of the clouds in this study, then the assumption of the C1 distribution should not greatly alter the model results.

For a given droplet distribution, the volume extinction coefficient depends on the liquid water content. Due to the short lifetime of the clouds studied, no liquid water content information was obtained for the five clouds scanned by the radiometer. Penetrations of surrounding clouds were made and liquid water content measurements were taken along the flight path with a Johnson-Williams liquid water content meter. Using time lapse flight films, several of the penetrated clouds which looked representative of the scanned clouds were chosen. The average liquid water content from 14 clouds penetrated at various levels was found to be $0.15\ g\,m^{-3}$ with a standard deviation of $0.06\ g\,m^{-3}$. This standard deviation gives some idea of the cloud to cloud variation of liquid water content, since it was found from 14 values, each of which was an average along the flight path of the aircraft. Each of these values was a small sample of the total liquid water content of each cloud. The variability of the liquid water content averaged over the entire volume of each cloud would probably be even less. The variability of liquid water content along each flight path was slightly greater. The average standard deviation of the liquid water content along each flight path was $0.08\ g\,m^{-3}$. The liquid water content values were recorded at a rate of one per second, and the groundspeed of the aircraft was about 80 $m\,sec^{-1}$. About 25 values would be recorded across a cloud 2 kilometers wide. The higher values of liquid water content did not appear to be located in any particular place along each flight path (for example near the center of the cloud). If the variations in liquid water content are randomly distributed throughout each cloud, a path through 25 regions of liquid water content with a standard deviation of $0.08\ g\,m^{-3}$ about a mean of $0.15\ g\,m^{-3}$ is approximately the same as an equal path through a homogeneous cloud with the same liquid water content. The value of $0.15\ g\,m^{-3}$ was assumed to be representative of an overall cloud average for each of the five clouds studied and was used as input for the Monte Carlo model.

The phase function and volume extinction coefficient also depend on the wavelength of the interacting radiation. The sensitivity of the radiometer was shown in figure 3. The maximum sensitivity is at a wavelength of about 0.8 μm with a half width of 0.3 μm. In equation (3.2) the volume extinction coefficient is given by the cloud liquid water content divided by a reference liquid water content, times a reference volume extinction coefficient. For the C1 distribution, the reference volume extinction coefficient is 16.73 km^{-1} at a wavelength of 0.7 μm and 17.29 km^{-1} at a wavelength of 1.19 μm. The general shape of the phase function for the C1 distribution does not vary greatly for wavelengths of 0.7 μm and 1.19 μm. Since both the reference volume extinction coefficient and the phase function do not vary greatly over the range of wavelengths the radiometer was sensitive to, the values at a wavelength of 0.7 μm were used in the model.

The single scatter albedo $\bar{\omega}_0$ is the probability that a photon will be scattered at each interaction ($1 - \bar{\omega}_0$ is the probability of absorption by a droplet). For the C1 droplet distribution, $\bar{\omega}_0$ has a value of 1.000 at a wavelength of 0.7 μm and a value of .9994 at 1.19 μm. Klehr and McKee (1978) presented results from a Monte Carlo model which included droplet absorption. For a cubic cloud with a C1 droplet distribution, an optical depth of 60 and a single scatter albedo of .9990 only about 5% of the incident energy on the cloud was absorbed. Since the single scatter albedo is even closer to 1.0 than .9990 over the whole range of wavelengths the radiometer was sensitive to, droplet absorption was neglected. Water vapor absorption was also neglected, although there is a weak water vapor absorption band near 0.8 μm. There is also a stronger water vapor absorption band near

0.93 μm, but this is in a region where the radiometer sensitivity is reduced. Molecular oxygen absorbs radiation with wavelengths around 0.76 μm. The absorption in this region is strong, but the absorption band is very narrow in wavelength compared to the wavelength interval to which the radiometer was sensitive. Also, the energy lost due to absorption by oxygen was about the same for each radiometer scan since the path lengths from the top of the atmosphere to the radiometer were similar. Since the energy absorbed was small and about the same for each scan, the effect of oxygen was also neglected.

The solar zenith angle θ_0 was computed and estimates of the cloud height and width were made from the slides taken just before each radiometer scan, as described in chapter 4. Each of the five clouds was modeled as a slab cloud with the height and width given by the average value estimated from the slides. For example, 11 measurements of the height and width of cloud 1 when viewed from different directions were made from the cloud slides. The average height of cloud 1 was 2.4 km with a standard deviation of 0.2 km (8% of the mean), and the width was 3.9 km with a standard deviation of 0.6 km (15% of the mean). These standard deviations give an idea of how much the cloud height changed from scan to scan and how much the cloud width varied when viewed from different directions. The maximum standard deviation of any height or width measurement of the five clouds studied was 21% of the mean. The vertical optical depth of each cloud is linear with vertical geometric distance since all the clouds were assumed to have a C1 droplet distribution and a liquid water content of 0.15 g m^{-3}. The average height and width, vertical optical depth (τ) and solar zenith angle θ_o for each cloud are shown in table 2. An average zenith angle was used for each cloud. In the time between the first and last radiometer scans of each cloud, the zenith angle did not change by more than 1.5 degrees.

5.2 Model radiance and radiometer scan comparison

As discussed in chapter 4, the angle from the horizontal projection of the solar beam to the direction from which the radiometer viewed the cloud (ϕ_s) was computed for each radiometer scan. Figure 12 shows how this angle was used to determine which model radiance each scan corresponded to. First, the angle ϕ_s was used to determine which face of the slab each scan corresponded to. If ϕ_s was between -45° and +45°, the scan was compared to results from the +Y side of the slab and if ϕ_s was between 45° and 135°, the scan was compared to results from the +X face, etc. The angle ϕ_s was then used to determine which 15° interval of the model azimuth angle ϕ the scan corresponded to. Each of the scans was actually compared to a weighted average of the model results from 2 of the 15° azimuth intervals. For example, if ϕ_s of a particular scan was equal to 45°, it was compared to the average of the model radiances from the ϕ_s interval of 30°-45° from the +Y face and the radiances from the ϕ_s interval of 45°-60° from the +X face. If ϕ_s of a particular scan was 37.5° it would then be compared to results from only one ϕ_s interval since it is in the center of the 30°-45° interval. Each vertical scan of the cloud corresponded to (in the coordinate system of the model) a fixed azimuth angle ϕ and varying zenith angle θ. It was assumed that each scan began with the radiometer approximately horizontal ($\theta = 90°$). As in figure 13,

Table 2. Input parameters for the Monte Carlo model

	Height (km)	Width (km)	$\frac{\text{Width}}{\text{Height}}$	τ (vertical)	θ_o
Cloud #1	2.4	3.9	1.6	96	21°
Cloud #2	3.0	4.2	1.4	120	24°
Cloud #3	0.8	1.4	1.8	32	20°
Cloud #4	1.6	2.6	1.6	64	24°
Cloud #5	1.5	2.7	1.8	60	28°

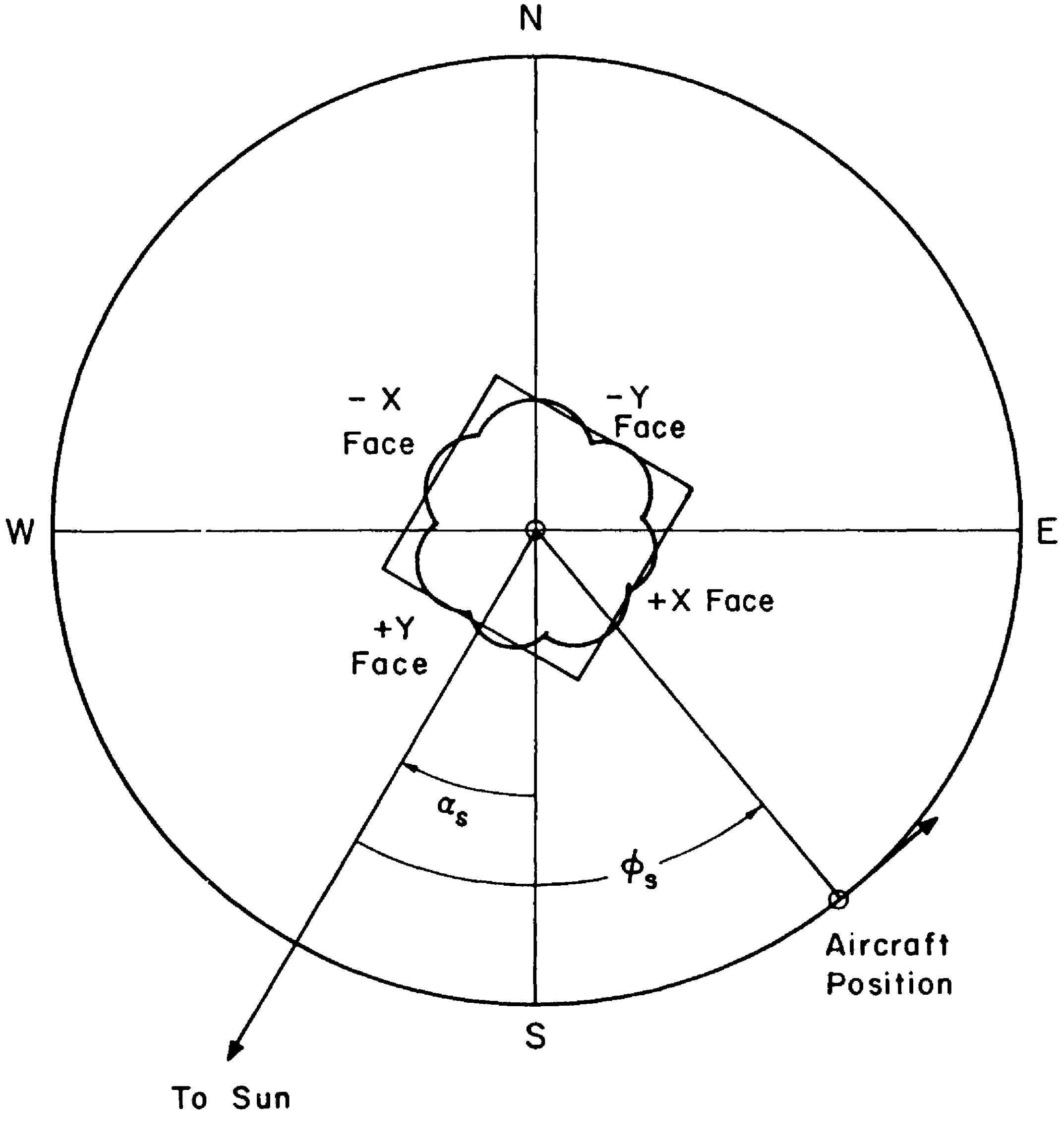

Figure 12. Relation between actual cloud and model cloud coordinate systems.

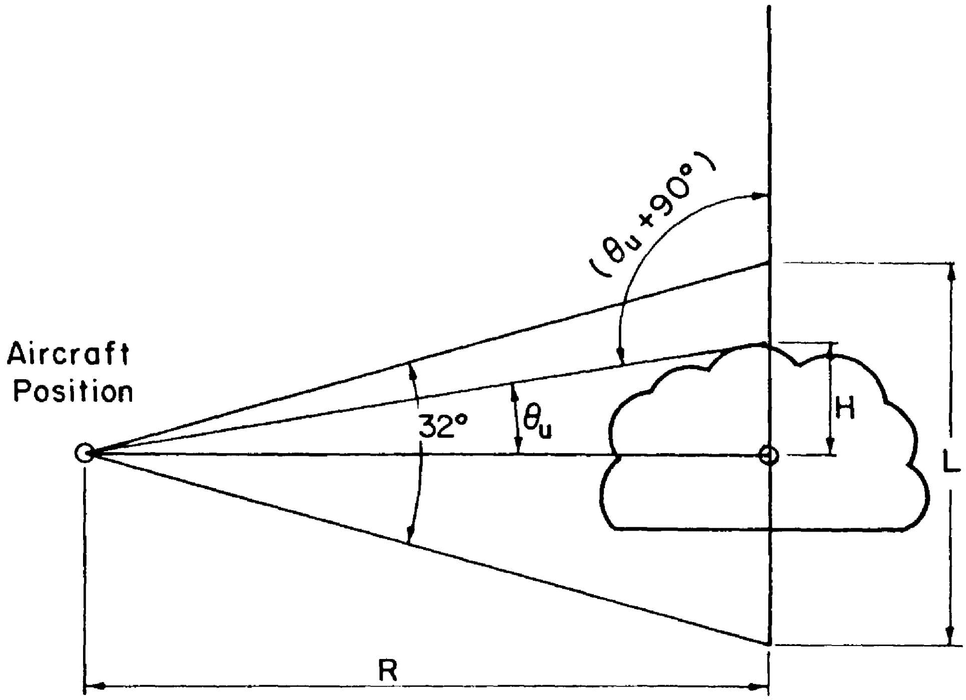

Figure 13. Estimation of the range in zenith angle of each radiometer scan from photographs.

when the radiometer field of view reached the top of the cloud, it was pointed upward at an angle θ_u which corresponds to a zenith angle of $90° + \theta_u$ in the coordinate system of the model. The angle θ_u was determined from the slide photographs. The vertical angular field of the camera is 32° and the slides are 24 mm from top to bottom. In figure 13, R is the aircraft to cloud center distance, H is the distance from the point on the cloud which is in the center of the slide to the cloud top and L is the distance that would be intercepted by a 32° field of view at a perpendicular distance R. From figure 13;

$$\tan \theta_u = \frac{H}{R} \tag{5.1}$$

and

$$\tan 16° = \frac{L}{2R} . \tag{5.2}$$

Dividing (5.1) by (5.2) and solving for θ_u gives

$$\theta_u = \mathrm{Tan}^{-1} \left(\frac{2H}{L} \tan 16° \right) . \tag{5.3}$$

The ratio of H/L is equal to h/24 mm where h is the distance measured in millimeters from the slide center vertically to the cloud top. Each vertical scan passed through a range of zenith angles from 90° to $(90° + \theta_u)$. A typical value of θ_u was about 12°. Since cos(90°) is zero and cos (102°) is about -0.20, this corresponds to a $\Delta(\cos \theta)$ of 0.20. Since the model radiances are defined in terms of a $\Delta(\cos \theta)$ of 0.05, each radiometer scan corresponds to a scan through about 4 solid angle boxes.

Before the radiometer scans are compared with the corresponding model radiances, the relation between the radiometer scans and the model radiances is discussed. In figure 14, a radiometer with a small

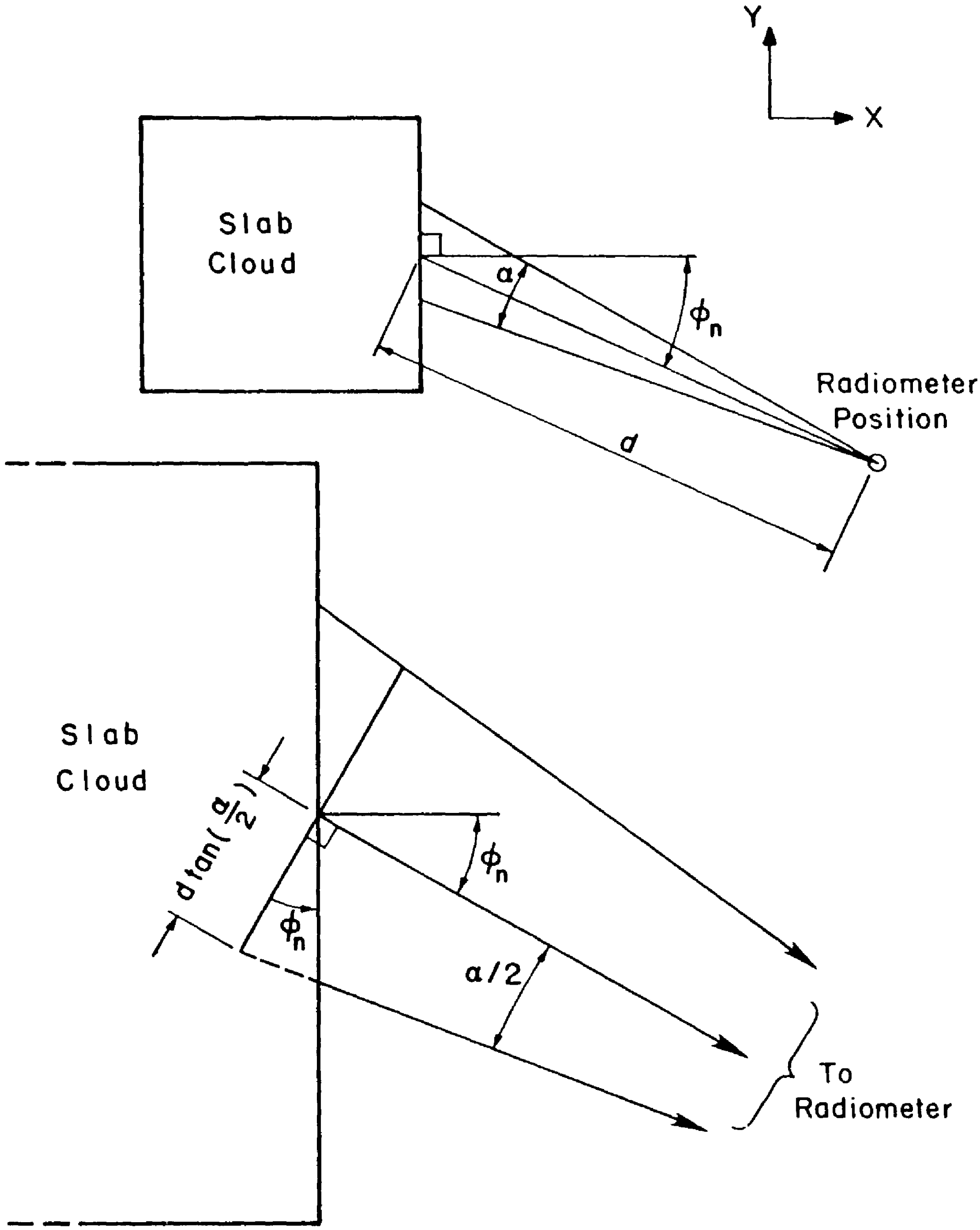

Figure 14. A radiometer viewing the side of a slab cloud.

field of view α views the side of a slab cloud from a distance d at an angle of ϕ_n from the normal to the slab face. Figure 14 is a top view of the slab cloud, so that the plane of the page is a horizontal plane. As in equation (3.12), radiance is given by

$$N = \frac{\text{Power}}{\Delta A \ \Delta\omega \cos \phi_n} \tag{5.4}$$

where ΔA is the area of a slab face, $\Delta\omega$ is a finite solid angle given by (3.9) and ϕ_n is the angle between the direction of the exiting photons and the normal to the cloud face. The power per unit area and solid angle which leaves the slab face into the direction the radiometer is pointed is then

$$\frac{\text{Power}}{\Delta A \ \Delta\omega} = N \cos \phi_n \ . \tag{5.5}$$

At a distance d, the radiometer field intercepts a circular spot with a radius of d $\tan \frac{\alpha}{2}$ as in the bottom of figure 14. The area of this circle is then $\pi(d \tan \frac{\alpha}{2})^2$. The projection of this area onto the side of the slab (A_c) is the area divided by the cosine of the angle between the normal to this area and the normal to the cloud face, which is the angle ϕ_n. The power per unit solid angle which leaves the slab face in the direction of the radiometer is then

$$\left(\frac{\text{Power}}{\Delta A \ \Delta\omega}\right)(A_c) = N \cos \phi_n \left[\frac{\pi(d \tan \frac{\alpha}{2})^2}{\cos \phi_n}\right]$$

$$\frac{\text{Power}}{\Delta A \ \Delta\omega} \ (A_c) = N \pi \ d^2 \tan^2 \frac{\alpha}{2} \ . \tag{5.6}$$

The radiometer intercepts the part of this power which passes into the small solid angle given by a_s/d^2 where a_s is the area of the radiometer sensor projected onto a sphere of radius d. Since the sensitivity of the radiometer sensor is not the same over the entire sensor area, the solid angle is actually given by $\frac{a_e}{d^2}$ where a_e is the area of a sensor which intercepts the same amount of power as a_s, but has a sensitivity of unity over its entire area. The power which the radiometer intercepts (P_R) is then

$$P_R = \frac{\text{Power}}{\Delta A \ \Delta\omega} (A_c) \frac{a_e}{d^2} = N \ \pi \ d^2 \ (\tan^2 \frac{\alpha}{2}) \frac{a_e}{d^2}$$

$$P_R = N \ \pi \ a_e \ \tan^2 \frac{\alpha}{2} \ . \qquad (5.7)$$

Since a_e and α are constants, the power the radiometer intercepts is proportional to the corresponding radiance given by the Monte Carlo output provided that the radiometer field of view is entirely on the cloud. It must be kept in mind that the Monte Carlo radiances are averages over an entire cloud face, while the radiometer intercepts only a small portion of the cloud surface.

Figures 15-17 show the actual radiometer scans and the corresponding model radiances for cloud 2. The Monte Carlo radiances were normalized to the actual scans so that the sum of the average of the radiometer scans would be equal to the sum of the average of the corresponding model radiances. The model radiances for the entire cloud were multiplied by the same normalization factor. Scans 1 and 2 were compared to the +Y face (solar face), scan 3 was compared to an average between results from the +Y and +X faces (since $\phi_s = 46°$), scans 4-5 and scans 10-13 were compared to either the +X or -X face (these two faces are symmetric), and scans 6-9 were compared to the -Y face.

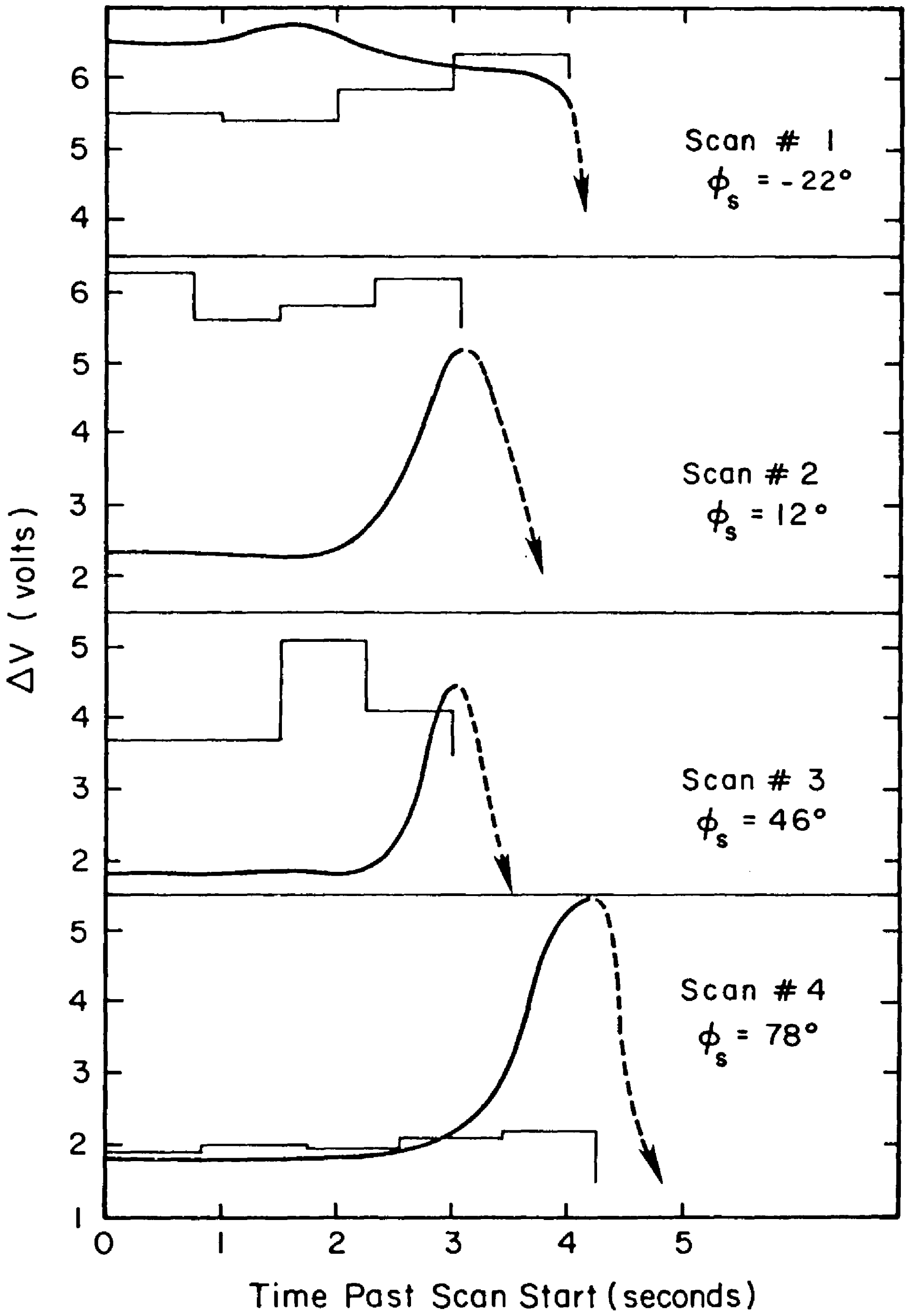

Figure 15. Comparison of radiometer scans and corresponding normalized model radiances for cloud 2, scans 1-4.

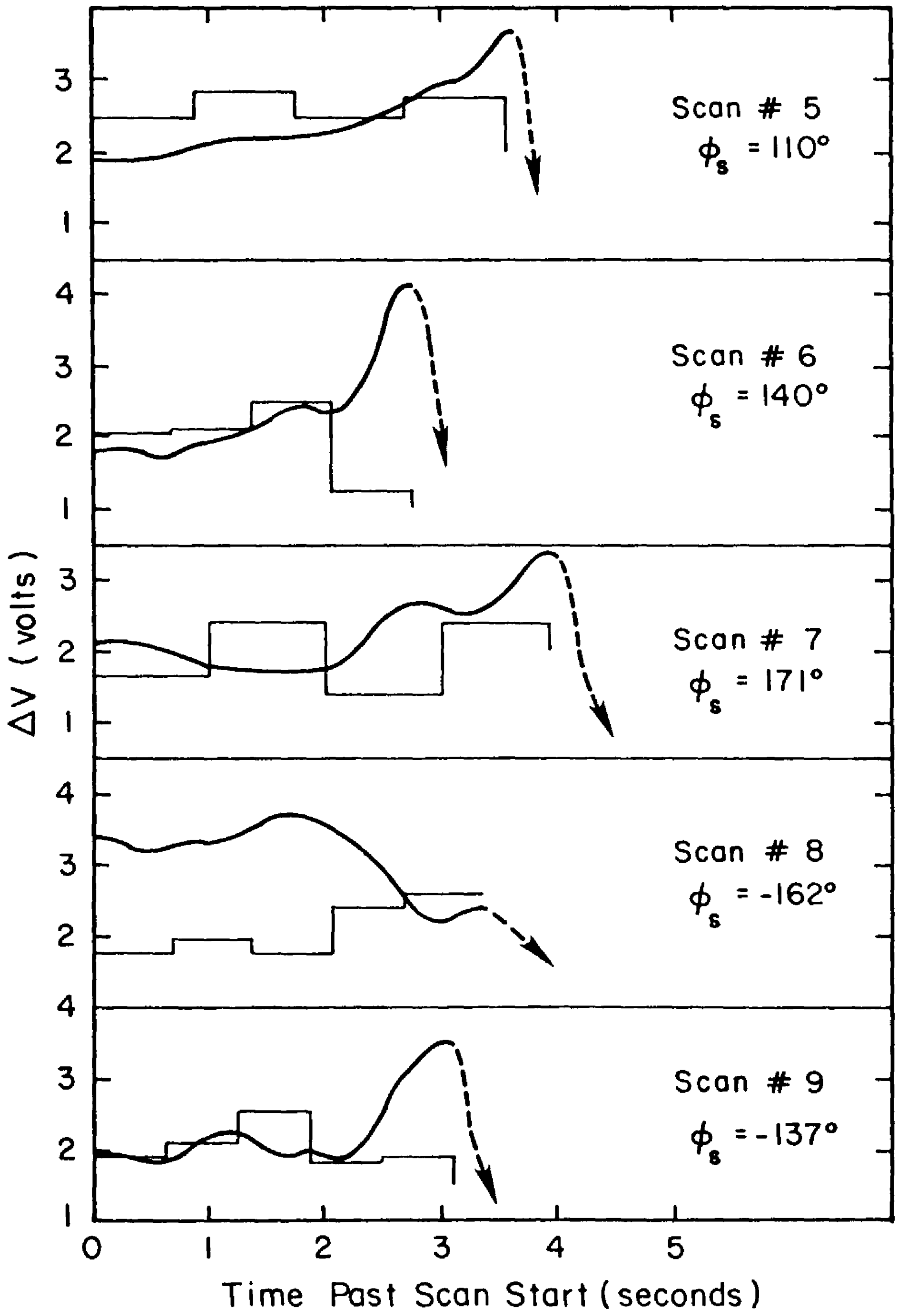

Figure 16. Same as figure 15 for cloud 2, scans 5-9.

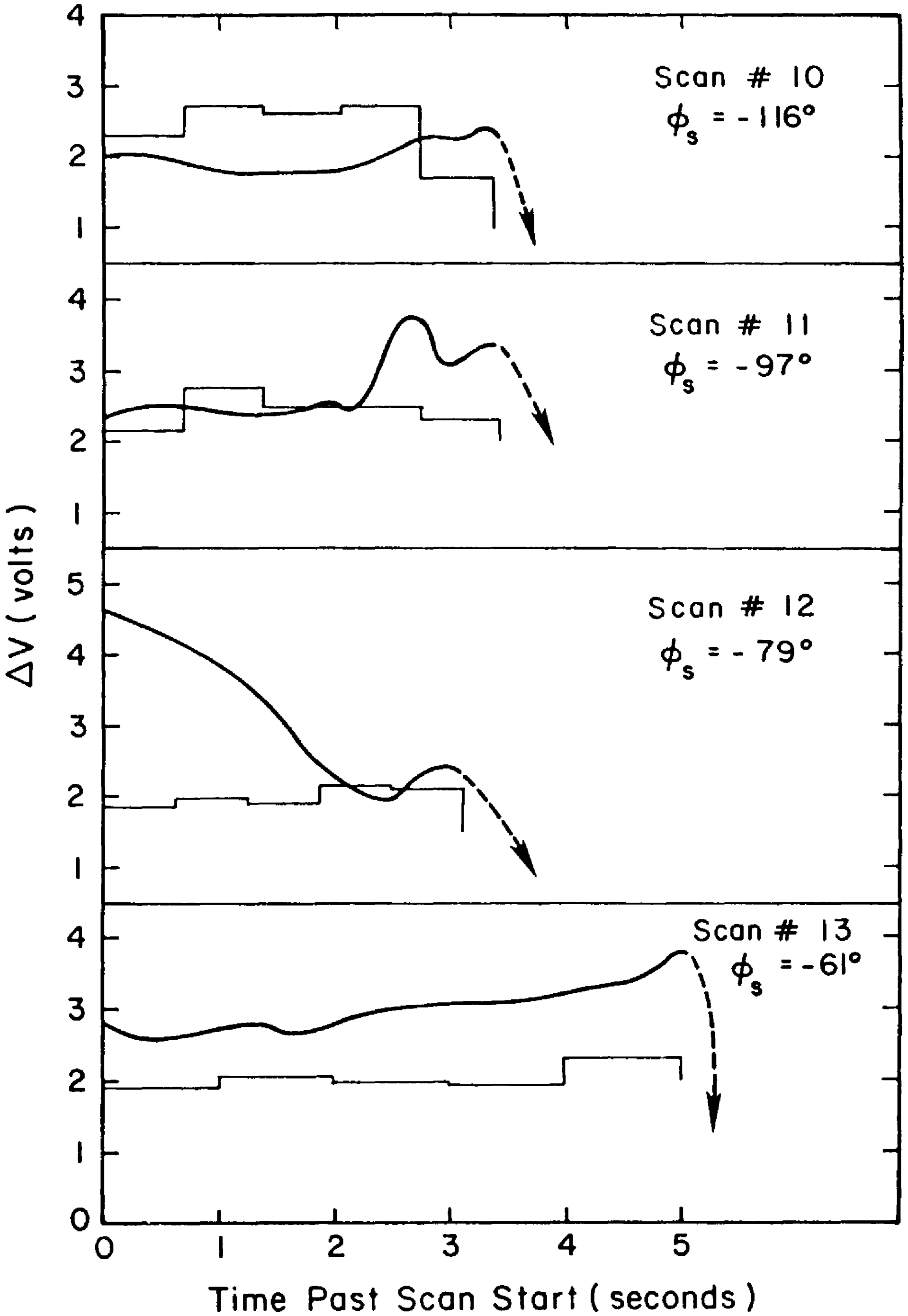

Figure 17. Same as figure 15 for cloud 2, scans 10-13.

Scan 1 is the brightest radiometer scan of this cloud, and is fairly uniform. The corresponding model radiances are also very bright, and vary slightly. Scan 2 begins in a dark region and passes through a bright region near the top of the cloud. This was caused by a feature on the cloud which shaded an area below it. Since the model assumes the cloud face is smooth, the effect of this feature does not show up. The shape of scan 3 is also affected by this cloud feature. The model radiances which correspond to scan 3 are not as bright as the model radiances for scans 1 and 2 since it was compared to an average of the results from the +Y and +X faces.

Scans 4-5 and scans 10-13 were compared to results from the +X or -X faces. The model radiances which correspond to these scans are relatively dark compared to the radiances from the +Y face. The actual radiometer scans vary quite a bit more than the model radiances. This is again due to smaller scale cloud features which the model does not include. Scan 4 is similar to scans 2 and 3 which were considered to be on or partially on the solar face. The end of scan 4 is very bright, which indicates that even at a ϕ_s of 78°, the cloud may still be receiving some direct sunlight. The corresponding model radiances do not show this increase at the end of the scan since the +X face does not receive any direct sunlight. This indicates that corner effects in the model may be important in some cases.

Scans 6-9 were compared to the -Y face of the slab (the antisolar side). All these radiometer scans except scan 8 show a maximum in radiance at the top of the cloud. This is due to the strong forward scattering peak in the scattering phase function as in figure 4. Photons which enter the top edge of the cloud and exit after only a few interactions leave the cloud in approximately the same direction as they entered. This results in a bright cloud edge on the antisolar side of the cloud. This does not show up in the corresponding model radiances due to the averaging of the model radiances over an entire cloud face. Even if a large number of photons exited the top edge of the antisolar slab face into a particular solid angle, these would be averaged with the area of the rest of the slab face where fewer photons exited into the same solid angle.

Each of the radiometer scans in figures 15-17 corresponded to a scan through about 4 or 5 solid angle boxes. Each of the radiometer scans was broken down into either 4 or 5 segments, and the radiometer voltage was averaged over each of these segments. The average of the radiometer voltage over each of the segments was then correlated with the radiance value from each of the corresponding solid angle boxes. A linear regression resulted in a correlation coefficient (r) of 0.47. The square of the correlation coefficient (r^2) can be interpreted as a measure of the variance of a variable that has been accounted for by the linear relationship with another variable. In this case, the model radiances account for only about 22% of the variance of the radiometer scans. This is not surprising since the radiometer field of view intercepts a circular area with a diameter of about 1/20 of the cloud height. The shape of a scan of areas of this size is controlled by the smaller scale cloud features, and was not expected to compare well with results from a model which considers a cloud to be a slab with smooth faces. The results from this type of comparison for cloud 2 are representative of the rest of the clouds.

With the exception of scans 2 and 3, it appears that the average of each radiometer scan is similar to the average of the corresponding model radiances, but the shape of the actual scans and model radiances differ greatly. This indicates that if a larger area of the actual cloud is viewed, the effect of the smaller scale cloud features should become less important. An average of a radiometer scan would correspond to increasing the area of the cloud which was viewed. Before the average of the radiometer scans are compared to results from the model, the variability of the actual cloud radiance is discussed.

5.3 Variability of cloud radiance

As can be seen in figures 15-17, the radiometer scans of the actual cloud were more variable than the corresponding Monte Carlo radiances, due to the smaller scale cloud features and the way the model radiances are calculated. In order to get an idea of how much the actual cloud radiance does vary, a study of the cloud slides was done using Colorado State University's ADVISAR system which is described in detail in Brown (1978). Several of the cloud slides were converted to an array of digitized values in terms of film density. The film density is measured by transmitting visible light through the film. The intensity of the light transmitted through the darkest part of the slide is recorded and corresponds to a density value of 0, and the intensity of the light transmitted through the brightest part of the slide is recorded and corresponds to a density value of 256. The intensity of the light transmitted through the rest of the points on the slide are then converted linearly to a digitized value between 0 and 256. Each slide was converted into an array of 512 x 512 digitized values. About 200 x 300 of these points were on the cloud so that each point represents the radiance from an area with a diameter of about 10 m. A calibration was done to determine the relationship between the voltage output of the radiometer and the film density of the slides. A series of slides of several cumulus clouds were taken from the ground using the optically aligned camera. The radiometer voltage at the time of each picture was recorded. One slide of a particular cloud was digitized and the position of the radiometer on this cloud when each of the other pictures were taken could be determined from the other slides. The average of several digitized values which corresponded to the radiometer field of view was taken at each of the radiometer positions. In this way, the average of the digitized values of film density could be compared to the corresponding radiometer voltage for several points on the same slide. This relationship was roughly linear over the range of density values observed as long as the radiometer field of view was completely on the cloud. This relationship could not be determined accurately for the five clouds in this study, since only one point on the slide could be matched with a radiometer voltage. From the calibration slides, a difference of one volt from the radiometer corresponded to about 40-60 density units.

The digitized array of density values was computer accessible. Frequency distributions were made of the slides from 3 positions around clouds 2, 3 and 5 which are shown in figures 18-20, 21-23 and 24-26, respectively. Only points which were on the cloud were used in the frequency distributions. The horizontal axis is the film density scale and the vertical axis is the number of array points

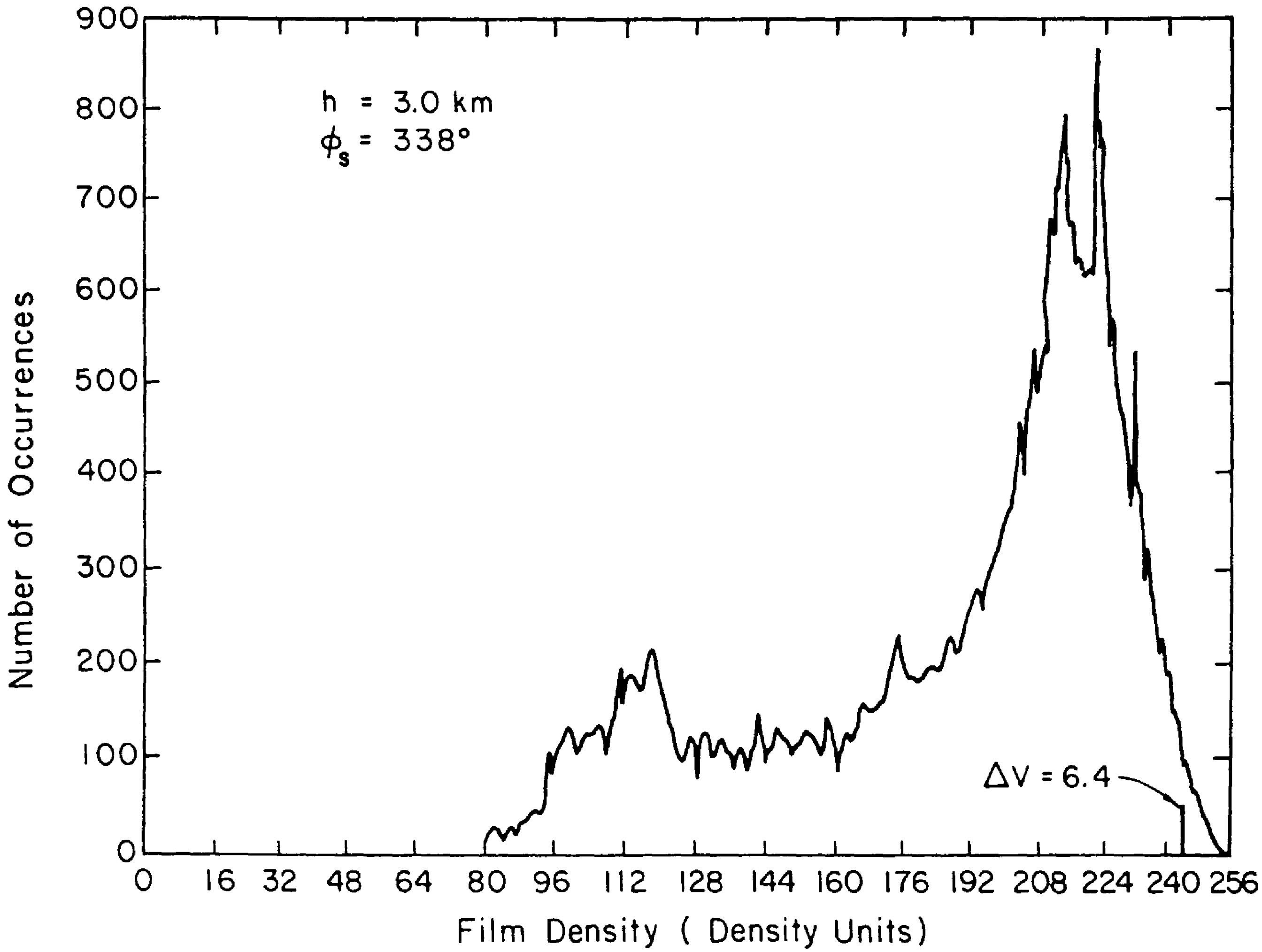

Figure 18. Frequency distribution for cloud 2, scan 1.

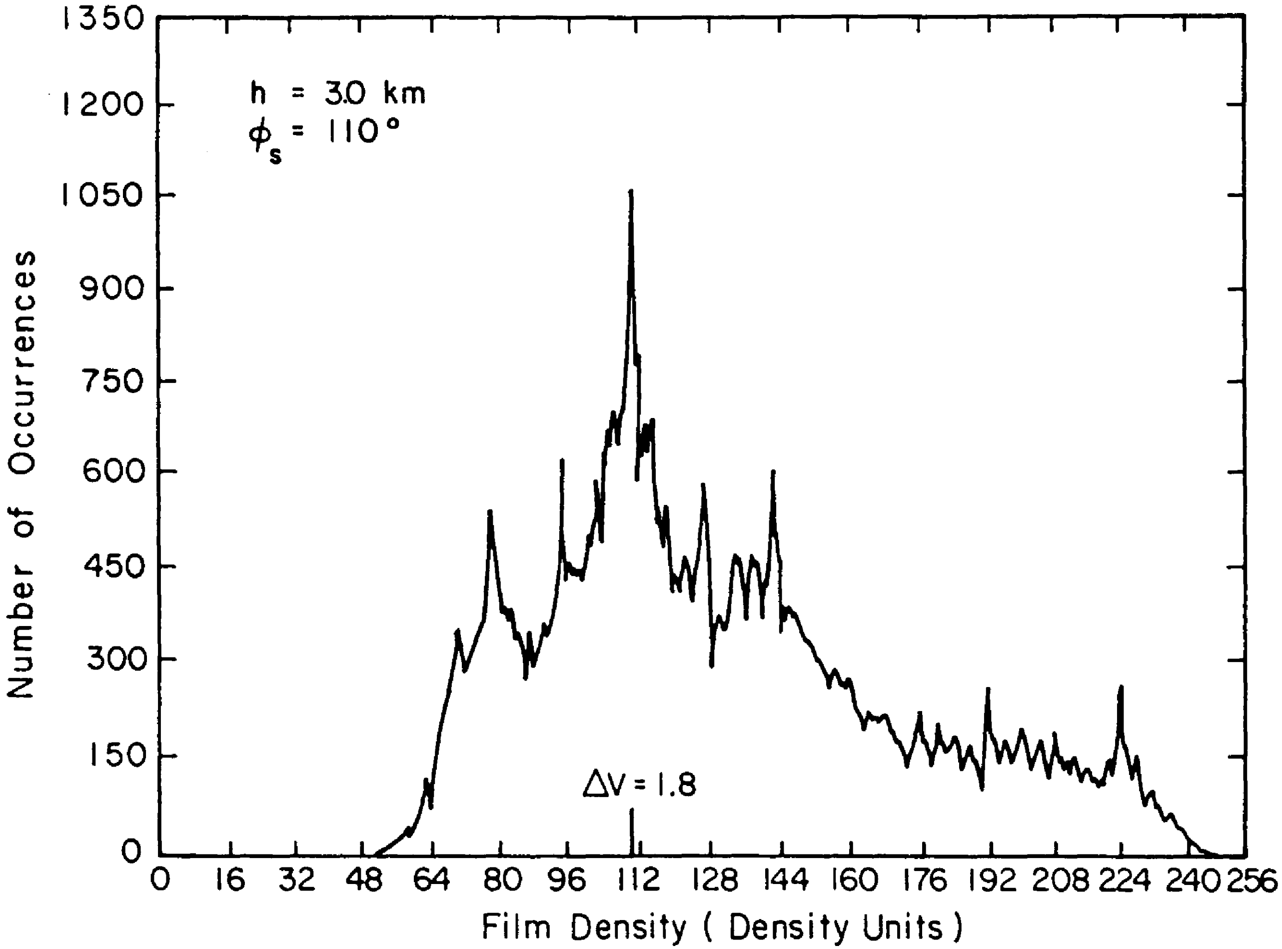

Figure 19. Frequency distribution for cloud 2, scan 5.

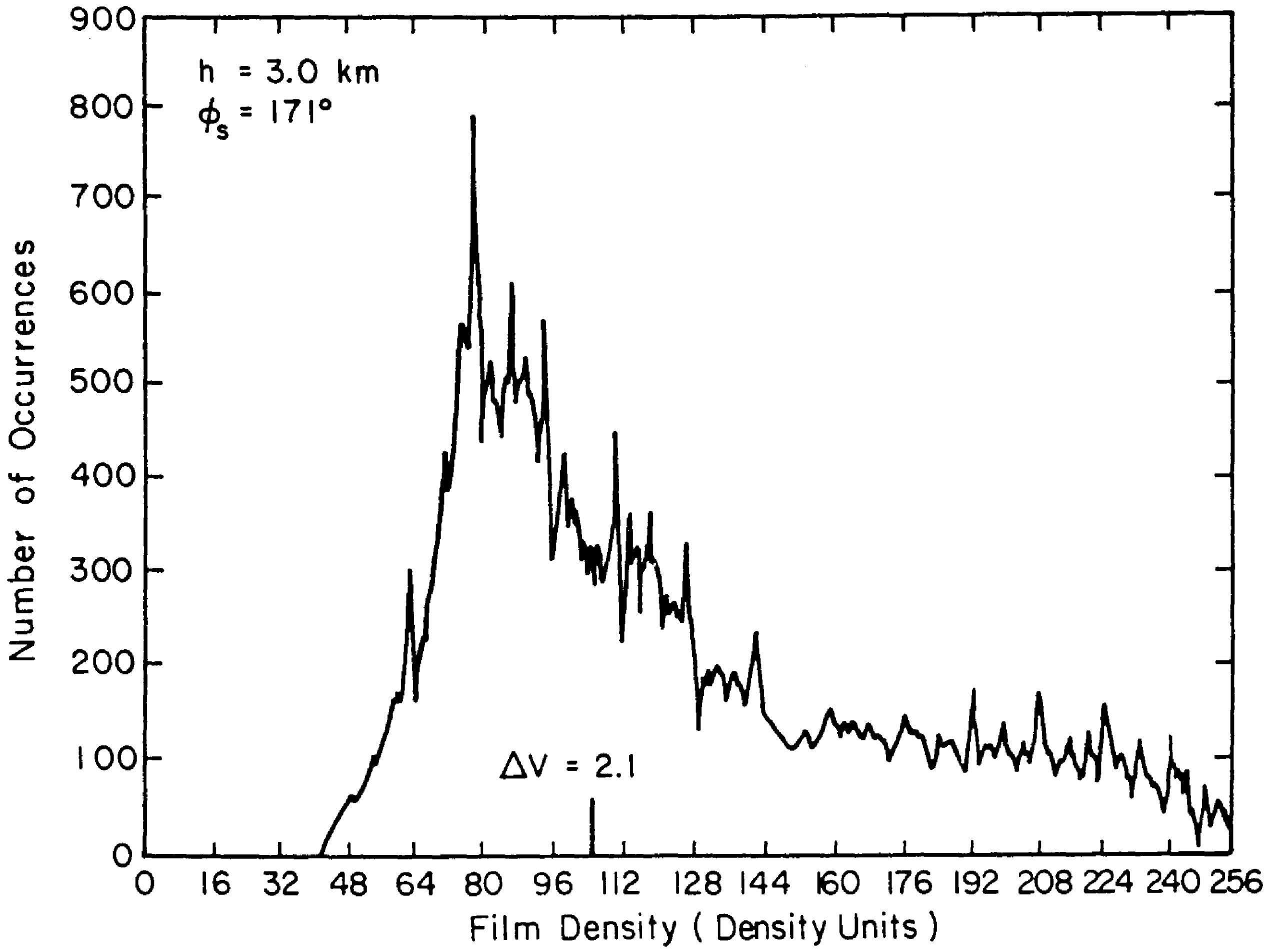

Figure 20. Frequency distribution for cloud 2, scan 7.

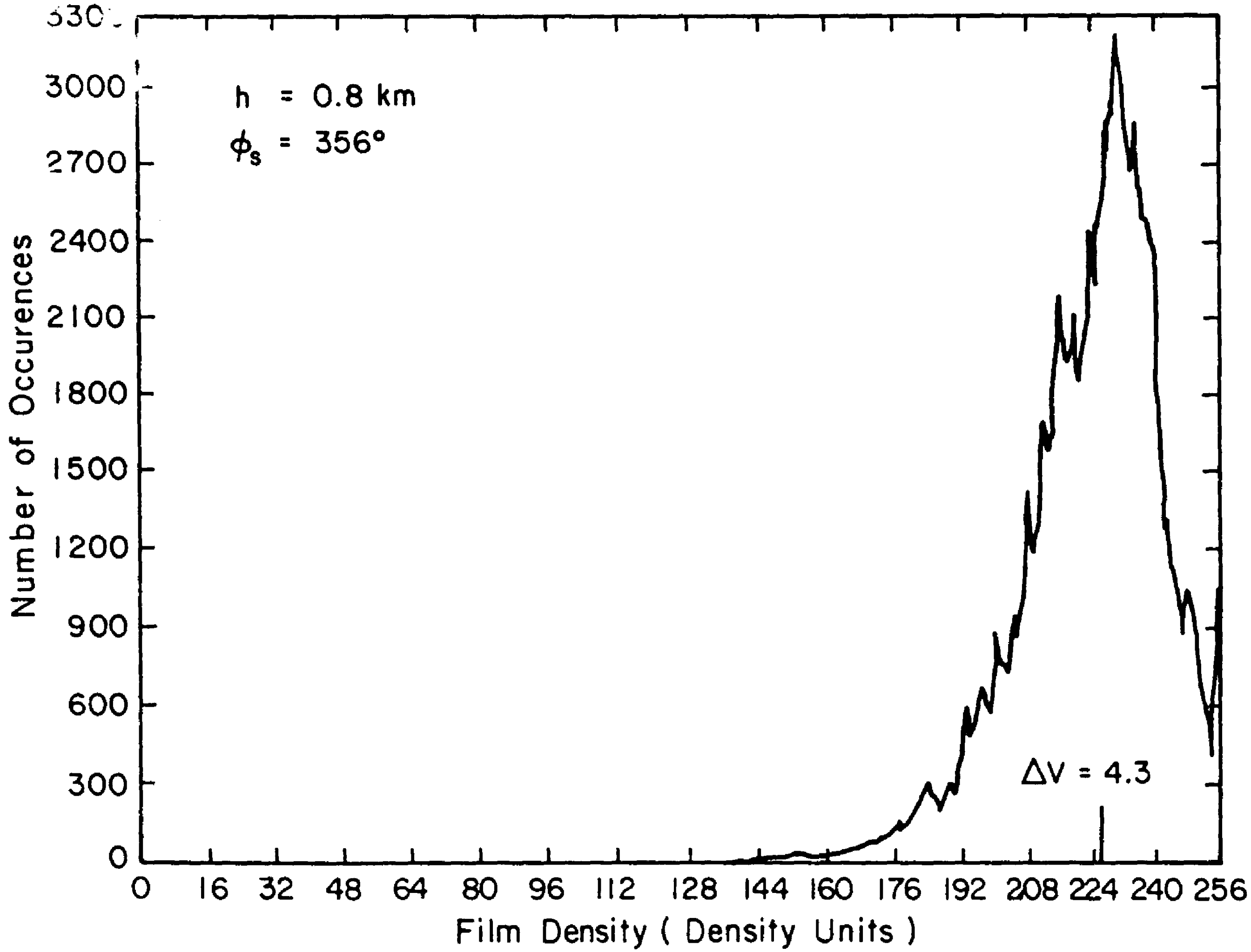

Figure 21. Frequency distribution for cloud 3, scan 2.

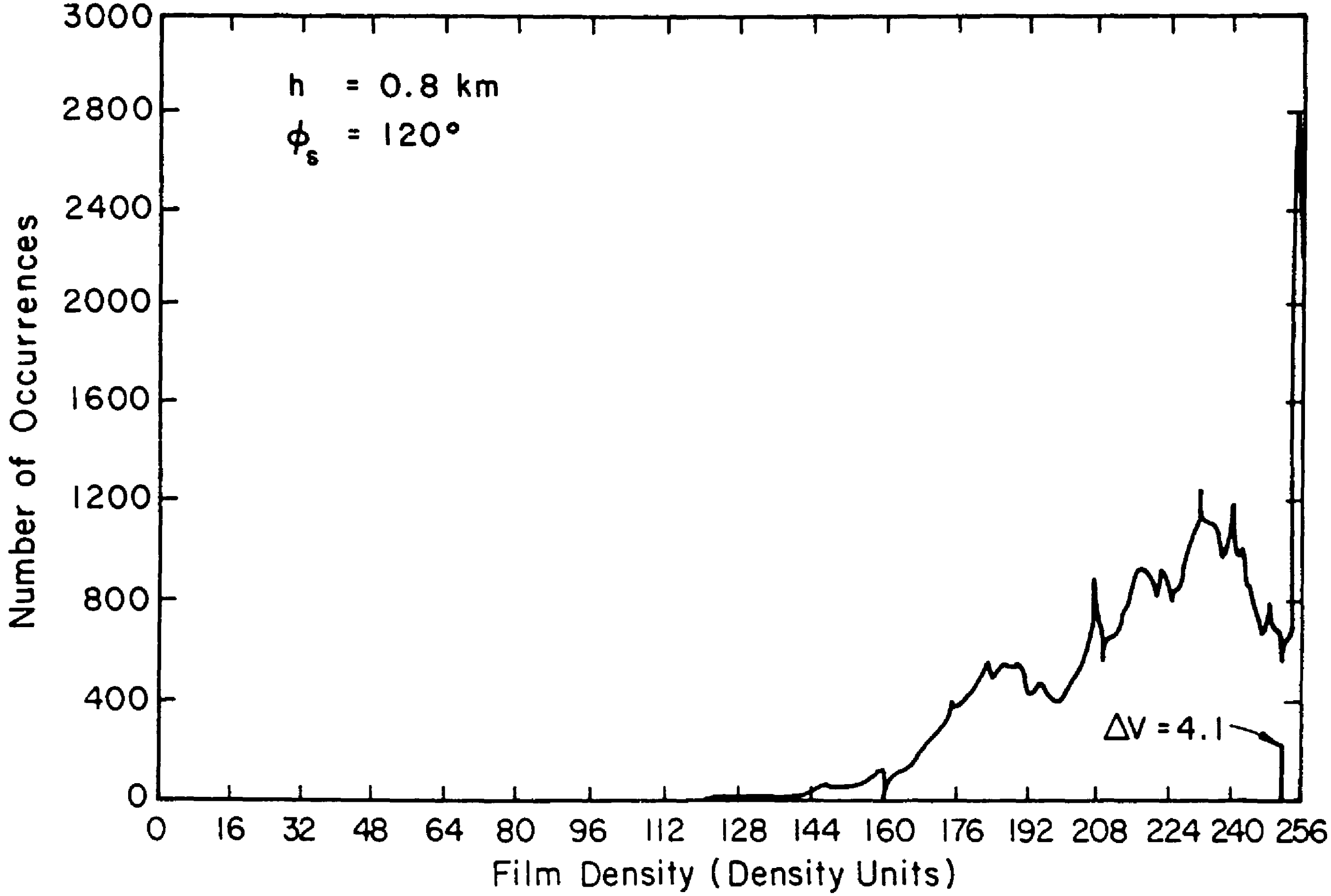

Figure 22. Frequency distribution for cloud 3, scan 4.

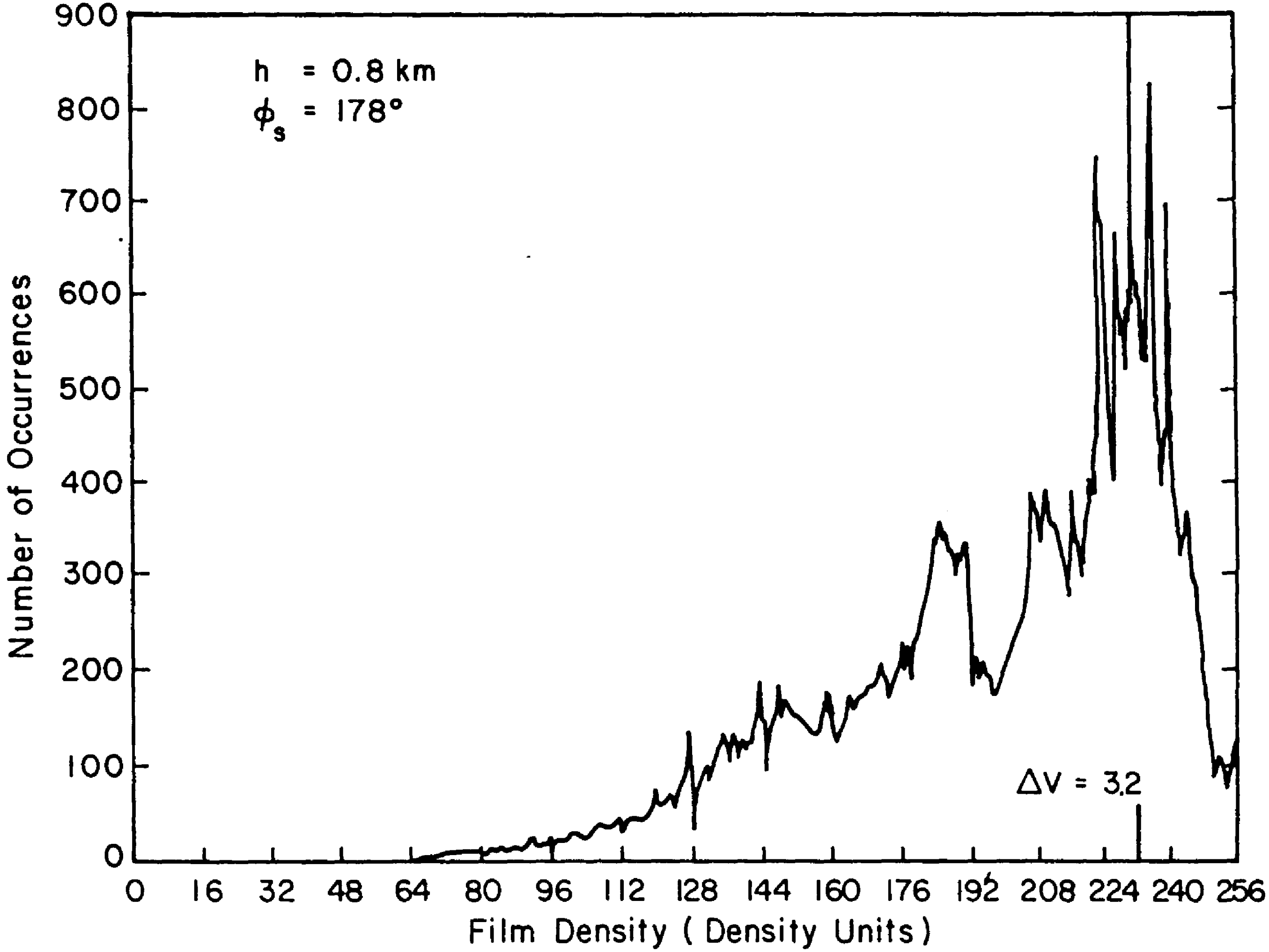

Figure 23. Frequency distribution for cloud 3, scan 5.

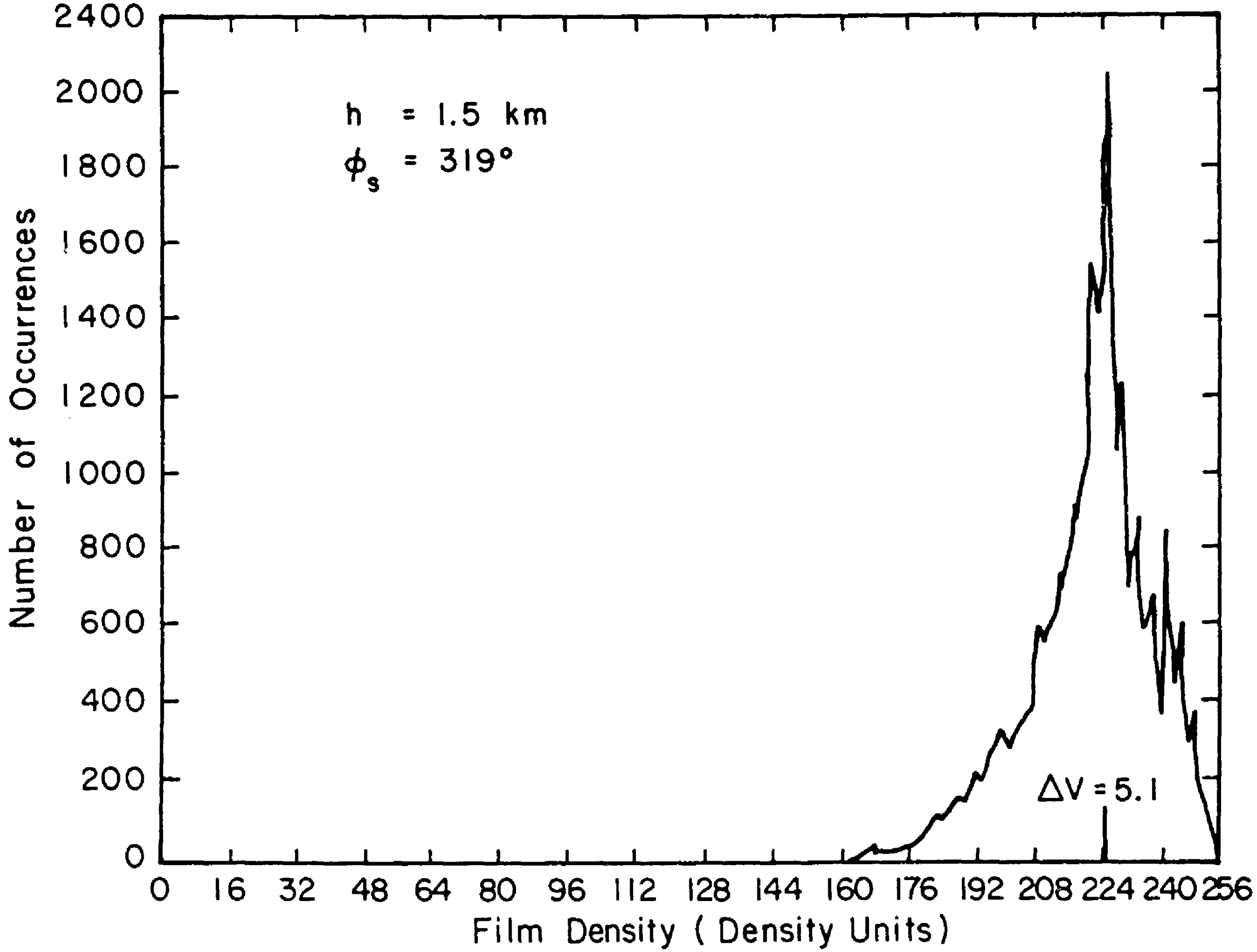

Figure 24. Frequency distribution for cloud 5, scan 4.

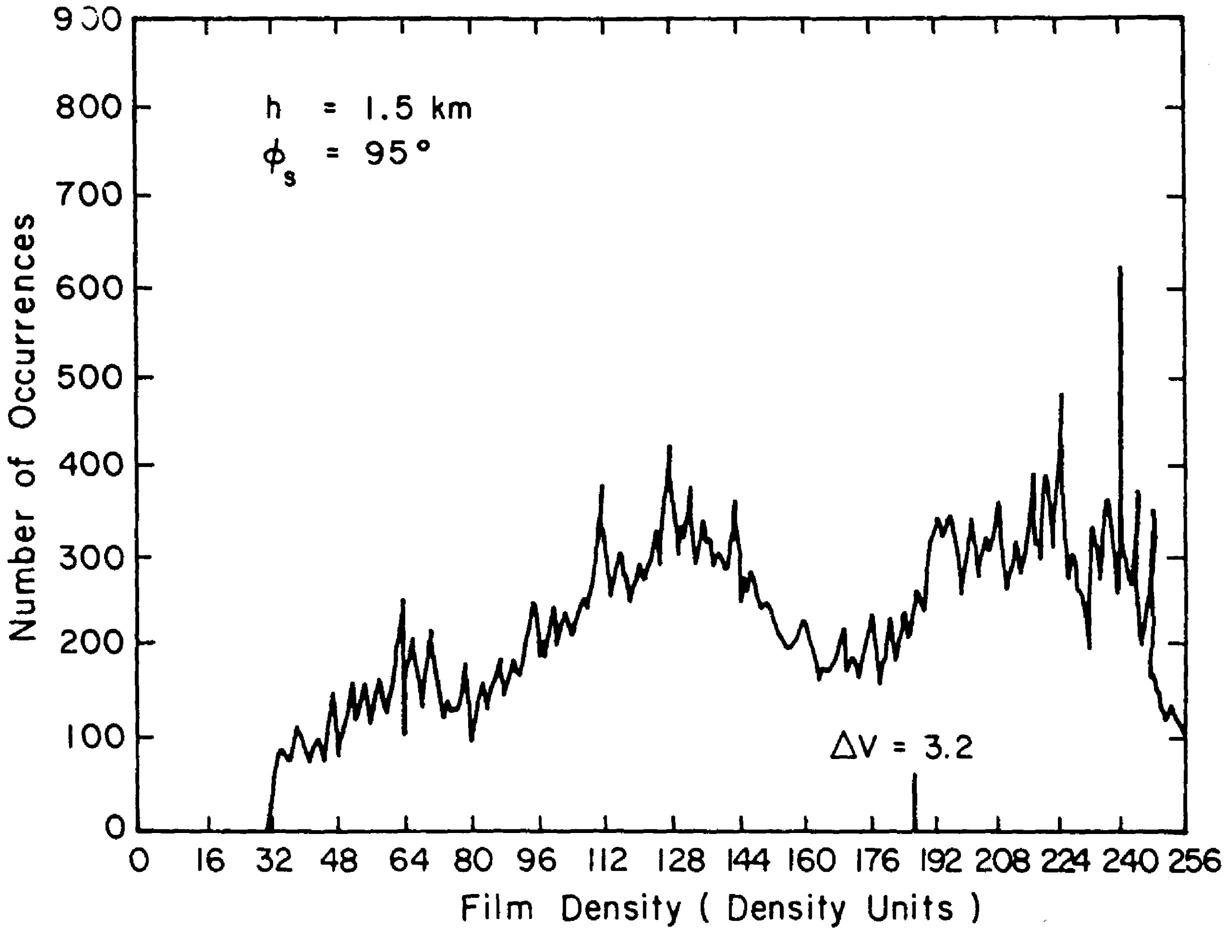

Figure 25. Frequency distribution for cloud 5, scan 1.

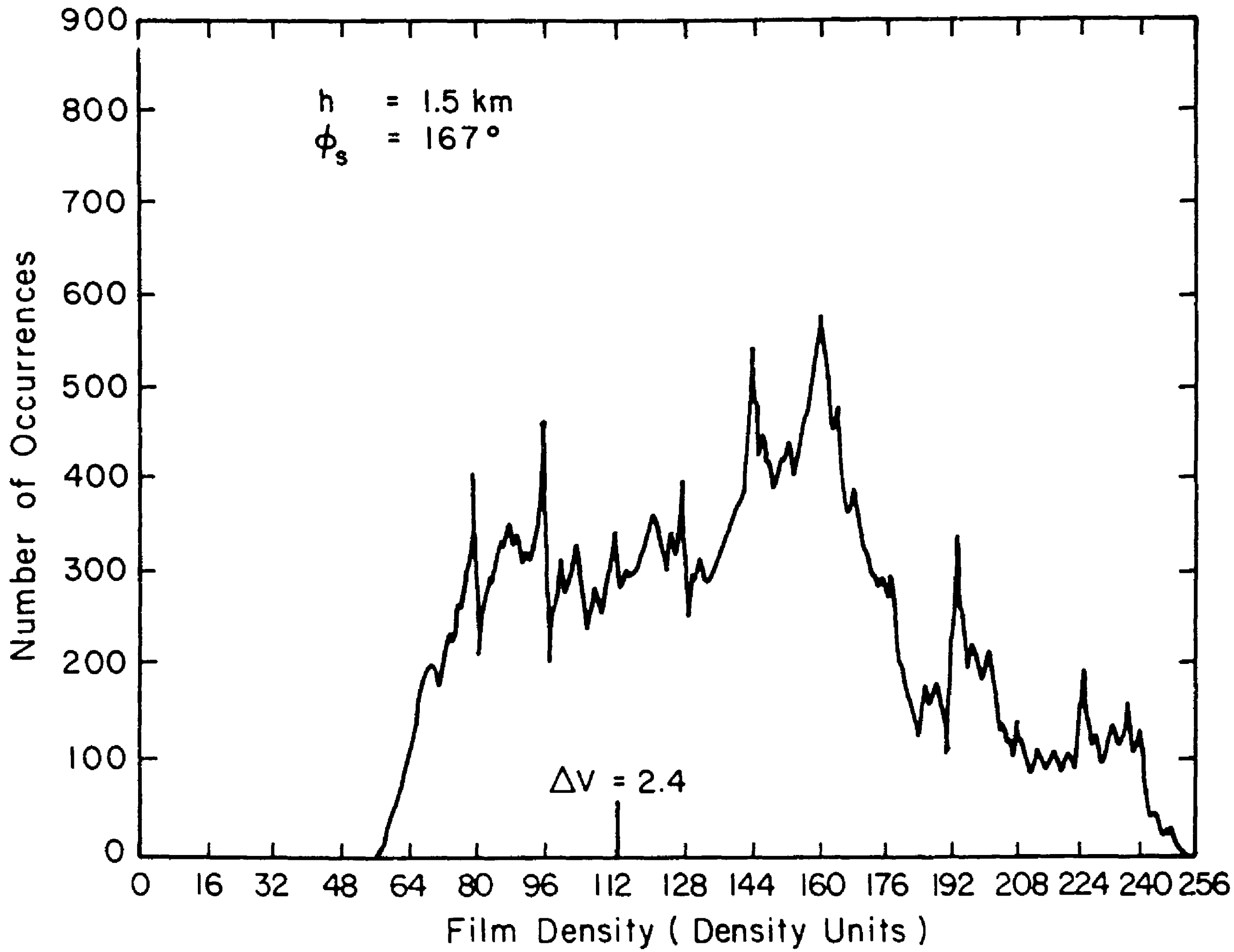

Figure 26. Frequency distribution for cloud 5, scan 2.

with a particular density value. For reference, the value of ΔV from the radiometer which corresponds to the density value at the center of each slide is shown in each diagram. For example, in figure 18, a density value of 244 corresponded to a ΔV of 6.4 volts. Since about 40-60 density units correspond to one volt, in this diagram a density value of about 200 corresponds to 5.4 volts. This relationship is not accurate enough to give quantitative results, but the general shape of each distribution gives a qualitative estimate of how the radiance varies. The height of each cloud and the angle ϕ_s from which the cloud was viewed are also shown in each figure.

Figures 18-20 show the frequency distributions for cloud 2, which is the largest cloud in this study with a vertical thickness of about three kilometers. Figure 18, which is the distribution of the slide taken from the solar side of the cloud, shows a large number of bright points while figures 19 and 20 show a larger number of darker points. All three distributions show some values over most of the range of density units. These are due to the smaller scale features of the cloud. In figure 20 (the distribution from the antisolar side of the cloud) the brightest points correspond to the bright edges of the cloud. On the average, the cloud radiance decreases from the solar side to the antisolar side, but there are some dark and bright areas in all three distributions. In figure 18, there is a small maximum near a density value of 112 units. This corresponds to a feature on the cloud which shades an area below it. In this case, it does not appear that this would greatly affect the average of all the density values, but would show up in a radiometer scan as a low value of ΔV.

Figures 21-23 show the frequency distributions for cloud 3 which is the smallest cloud in this study with a vertical thickness of about 0.8 kilometers. In figures 21 and 22, the range of density values is much less than for cloud 2. It appears that for a cloud of this size, the smaller scale cloud features are not optically thick enough to change the radiance of a particular cloud side very much. Figure 23 has a wider distribution, but it appears from the slide that the cloud was viewed from above in this case so that the cloud top was also visible. Most of the density unit values greater than about 200 are from the brighter cloud top. The average of the density values again decreases from the solar to the antisolar side of the cloud.

Figures 24-26 are the distributions for cloud 5 which has a vertical thickness of 1.5 kilometers. Figure 24 is from the solar side of the cloud and has a fairly narrow distribution. Figure 25 is the distribution of a slide taken 95° off from the direction of the incoming solar beam and has two distinct maxima. These are due to features on this part of the cloud which are partially illuminated and partially shaded from the sun. The parts of the cloud which are illuminated by the sun show up as the maximum near 224 density untis, while the shaded areas show up as the maximum near 128 density untis. A radiometer scan from this direction would be compared to model results from the +X face of the slab which is not directly illuminated by the sun. In this case, the radiometer scan would reflect these cloud features while the model would not. Figure 26 also has a wider distribution where the brightest points are due to the bright cloud edge on the antisolar side. The average of the density values also decreases from the solar to the antisolar side for this cloud.

In figures 18-26, the average of the density values from the slide of a particular cloud side is related to the sun and cloud orientation. The average of the density values decreases from the solar to the anti-solar side in each of the three clouds. The shape of each distribution was a measure of the variation in radiance of a cloud when viewed from a particular direction due to the smaller scale cloud features. The relative radiance of a cloud can vary by up to a factor of between four and five. In figure 20, for example, a density value of about 100 corresponded to a ΔV of 2.1. The range of density values on the cloud ranged from about 50 to 250. This corresponds to a range in ΔV from about 1.1 volts to 5.1 volts assuming that 50 density units equals 1 volt. The fourth radiometer scan of cloud 2 in figure 15 varied from a ΔV of 1.8 volts to 5.5 volts which was about a factor of 3 variation. A factor of five is an upper limit value for the radiance variations of the clouds studied. The frequency distributions from the smaller clouds were in general narrower than those of cloud 2. The variation in radiance was less for smaller clouds.

As shown in section 5.2, the radiometer scans of the actual clouds were much more variable than the corresponding model radiances due to the smaller scale cloud features. On a scale of 1/20 of the cloud height, the smaller scale cloud features still show up. If the field of view of the radiometer were gradually increased, at some point the smaller scale features should begin to average out. This process was simulated using the arrays of density values from three of the cloud slides. The resolution of the arrays was reduced by averaging sets of 4 array values together resulting in a new array with ¼ the number of points of the original array. This process was repeated several times, and the standard deviation of each array was found. Figure 27 shows the standard deviations from the arrays from 3 of the cloud slides. The abscissa is the diameter of the spot that each array value represented and the ordinate is the standard deviation of each array. The black circle is the radiometer spot size on each of the clouds. As can be seen in figure 27, the standard deviations of the arrays gradually decrease as the spot size increases. It appears that there is no critical size related to the decrease in radiance variations. The standard deviations are still quite high on the scale of the radiometer spot size. This indicates that the radio- could resolve many of the small scale cloud features. When each radiometer scan is averaged, the effect of the small scale cloud features should become less important, so that the average of each scan should be more representative of the average radiance of a cloud side. The results from this type of comparison are shown in the next section.

5.4 Comparison of scan averages

As described in section 5.2, the radiometer scans corresponded to a fixed azimuth angle ϕ, and a range in the zenith angle θ from 90° to about 102° in the model coordinate system. Each radiometer scan then corresponded to a scan through the four solid angle boxes defined by these angles. The average of the model radiances which correspond to an upward radiometer scan through these four solid angle boxes are shown in figures 28-32 for all values of ϕ_s between 0° and 180° for each cloud. Also shown in each figure is the vertical optical depth

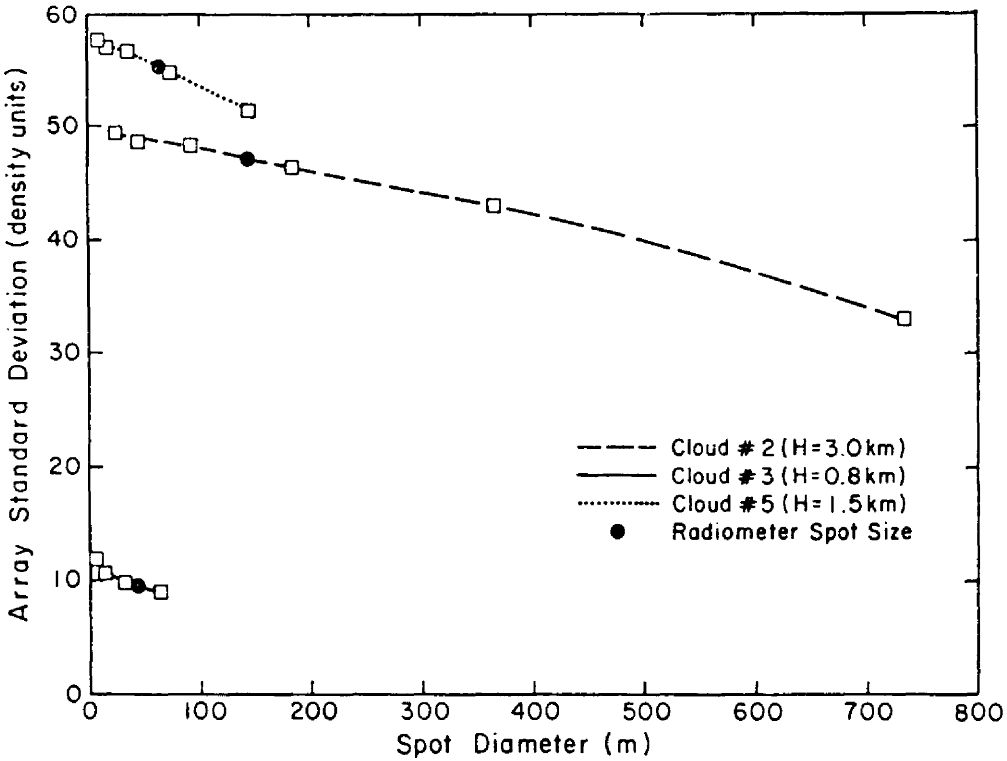

Figure 27. Array standard deviation versus spot diameter.

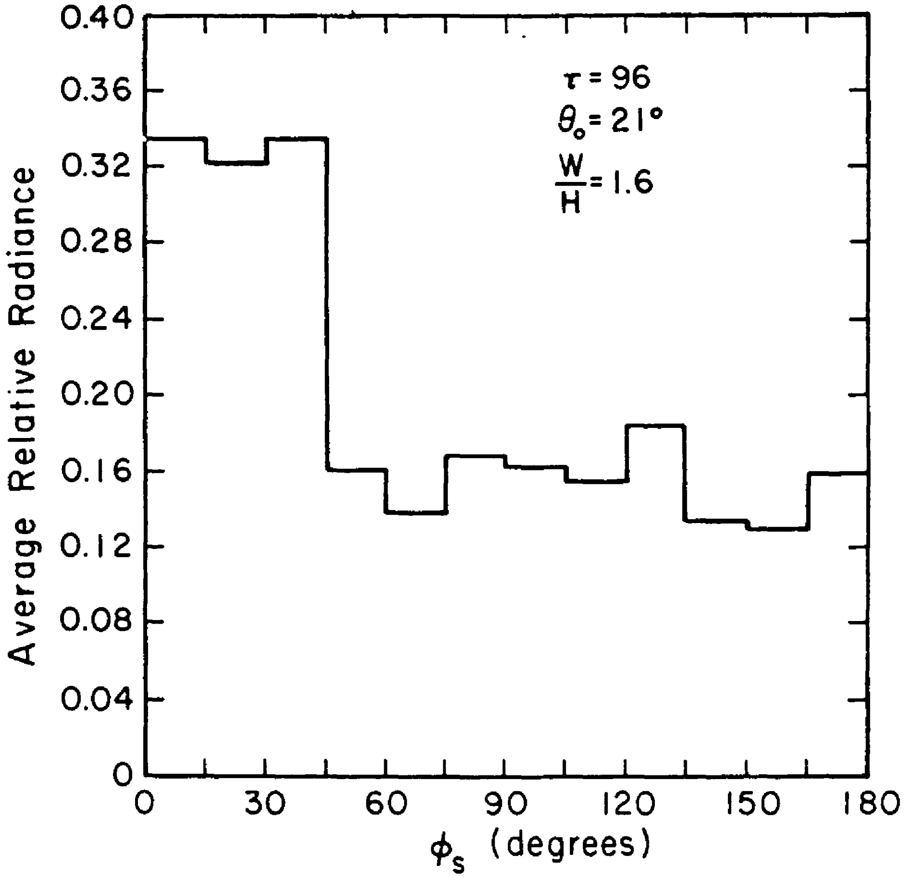

Figure 28. Average relative radiance of four solid angle boxes versus ϕ_s for the model of cloud 1.

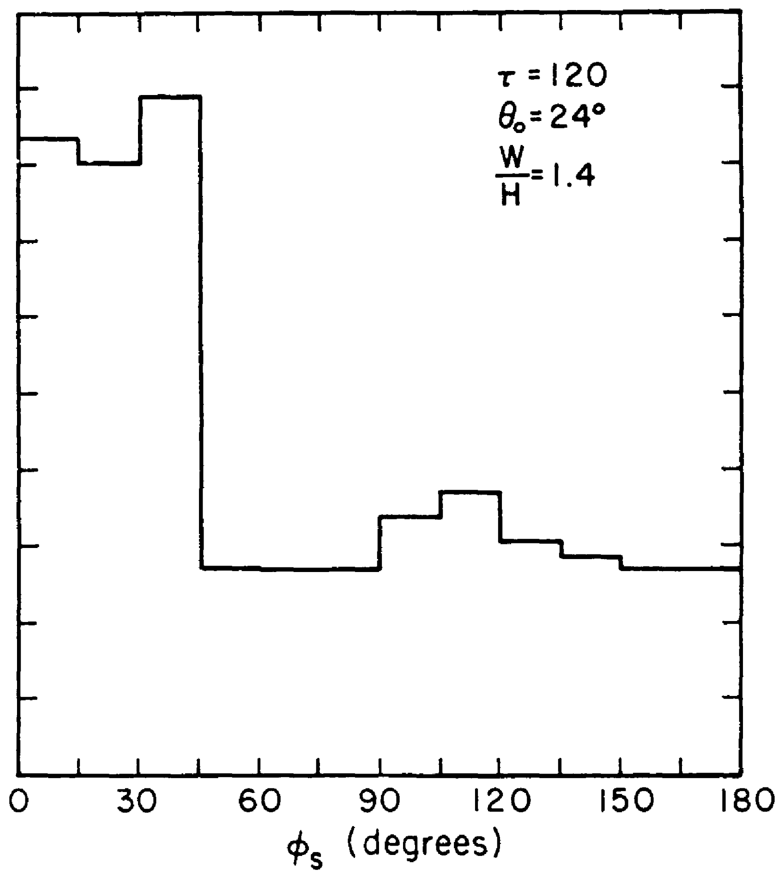

Figure 29. Same as figure 28 for the model of cloud 2.

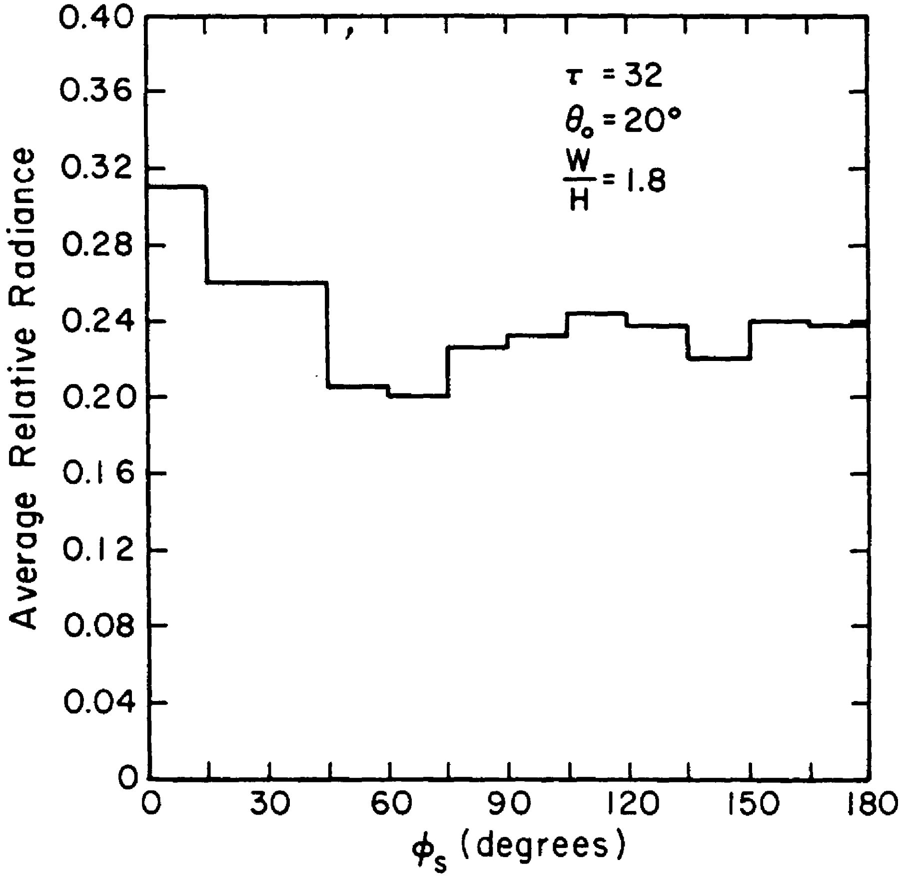

Figure 30. Same as figure 28 for the model of cloud 3.

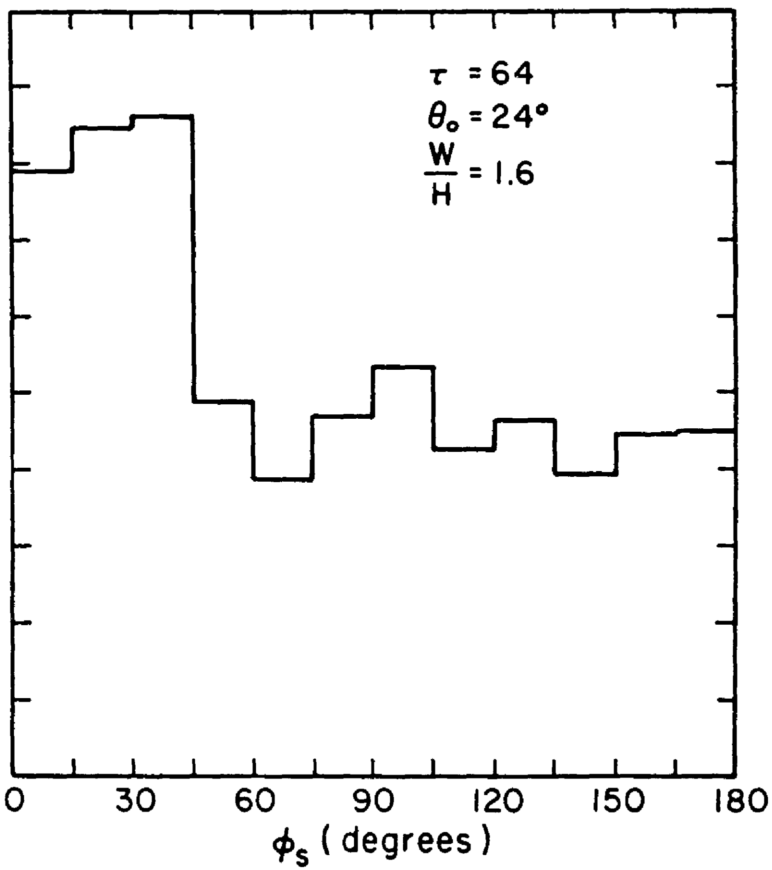

Figure 31. Same as figure 28 for the model of cloud 4.

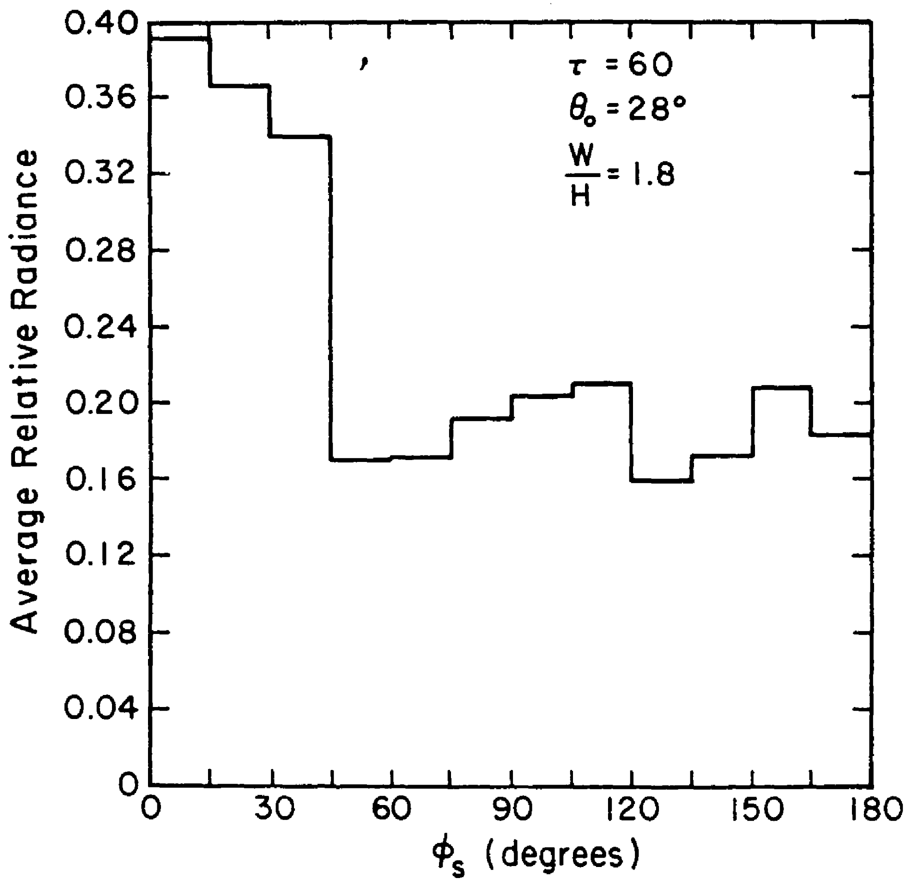

Figure 32. Same as figure 28 for the model of cloud 5.

τ, the ratio of cloud width to height W/H and the solar zenith angle θ_o. The shape of the radiance versus ϕ_s curve is similar for all five clouds. The radiances on the solar side of each cloud (when ϕ_s is between 0° and 45°) are much greater than on the other sides. All five clouds show some evidence of a smaller maximum radiance when ϕ_s is between 75° and 135°. With the exception of cloud 2 there is also some indication of a small maximum when ϕ_s is between 150° and 180°. The model radiances are symmetric about 180° so only the values between 0° and 180° are shown. The major difference between each of the clouds is the magnitude of the radiances on the solar side and the average of the radiances on the other two sides shown. As τ increases from 32 to 64 (figures 30 and 31), the solar side becomes brighter while the other sides become darker. There is not much change on the solar side as τ increases from 64 to 120 (figures 31 and 29) although the other sides become slightly darker. Other differences between the model clouds are due to the small differences between the solar zenith angles and the width to height ratios. For example, the solar side of cloud 5 (figure 32) with a τ of 60 is brighter than the solar side of cloud 2 with a τ of 120. This difference is due to the increased solar zenith angle. As the solar zenith angle increases, a greater portion of the incident photons enter the side of the slab.

In order to decrease the effect of the small scale cloud features, each of the actual cloud scans was averaged. Figures 33-37 show the average of the radiometer scans and the corresponding model radiances at various positions around each cloud. The model radiances were normalized to the radiometer scans so that for each cloud, the sum

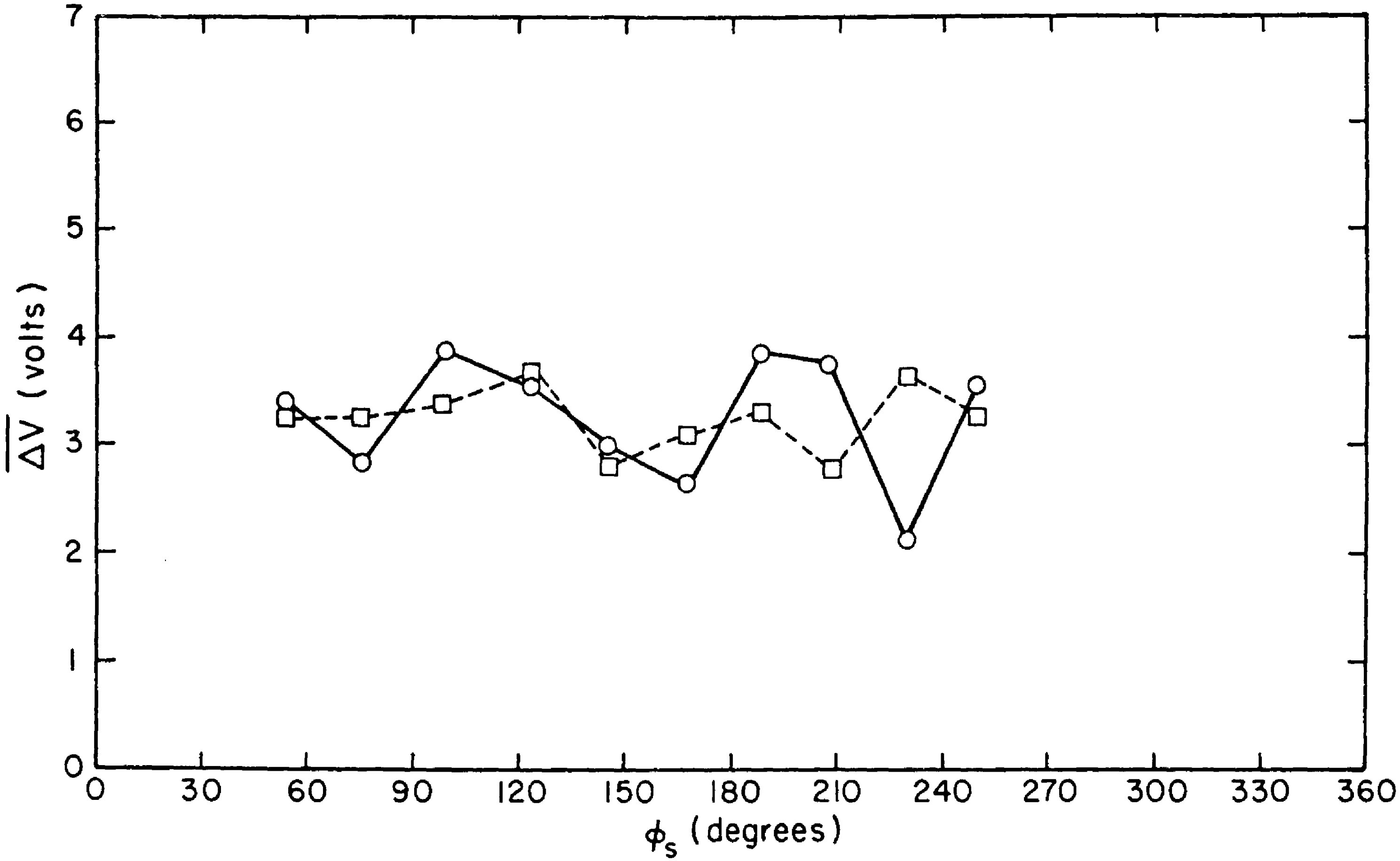

Figure 33. Comparison of radiometer scans and normalized model radiances for cloud 1 (Radiometer scans (circles), model radiances (squares)).

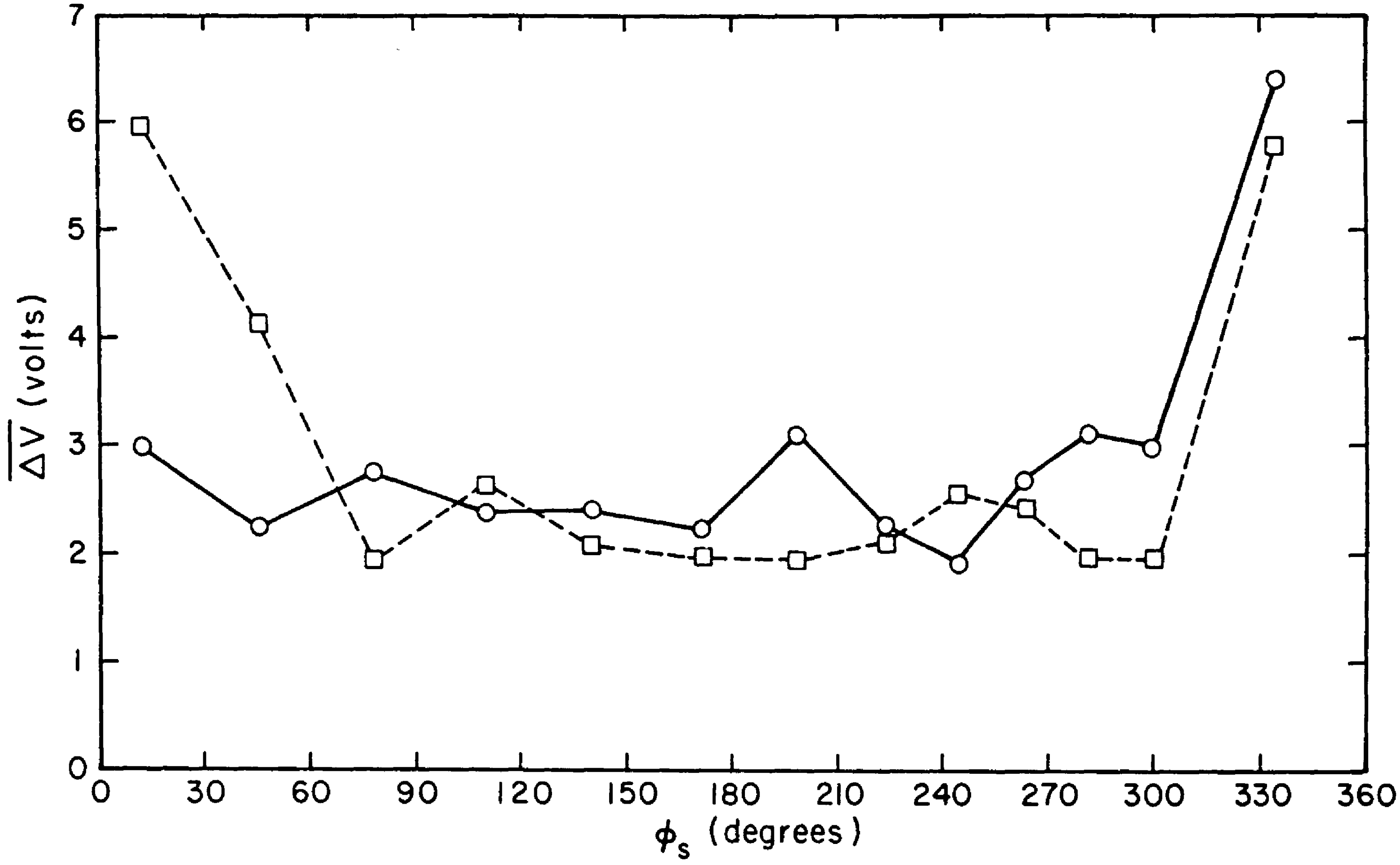

Figure 34. Same as figure 33 for cloud 2.

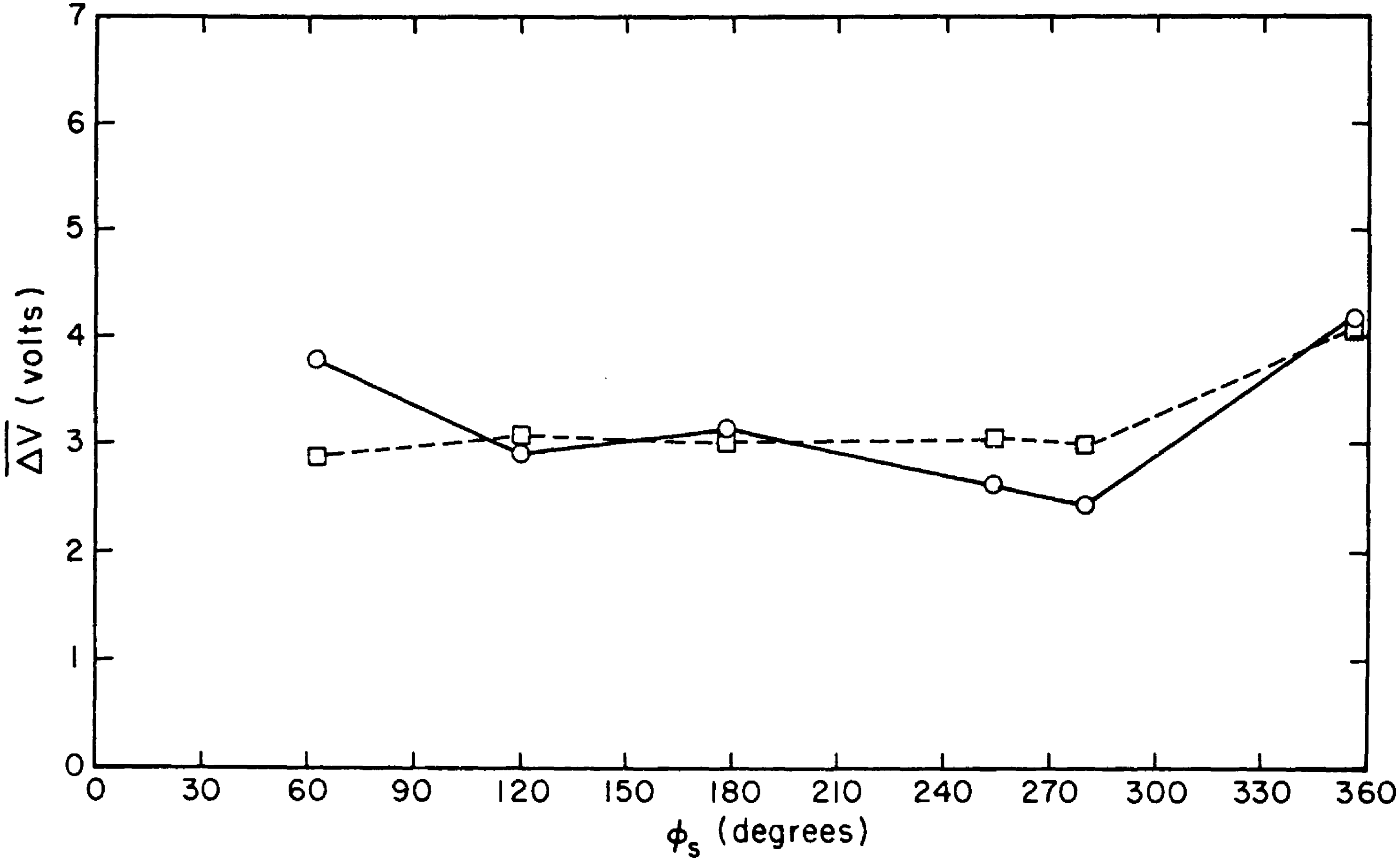

Figure 35. Same as figure 33 for cloud 3.

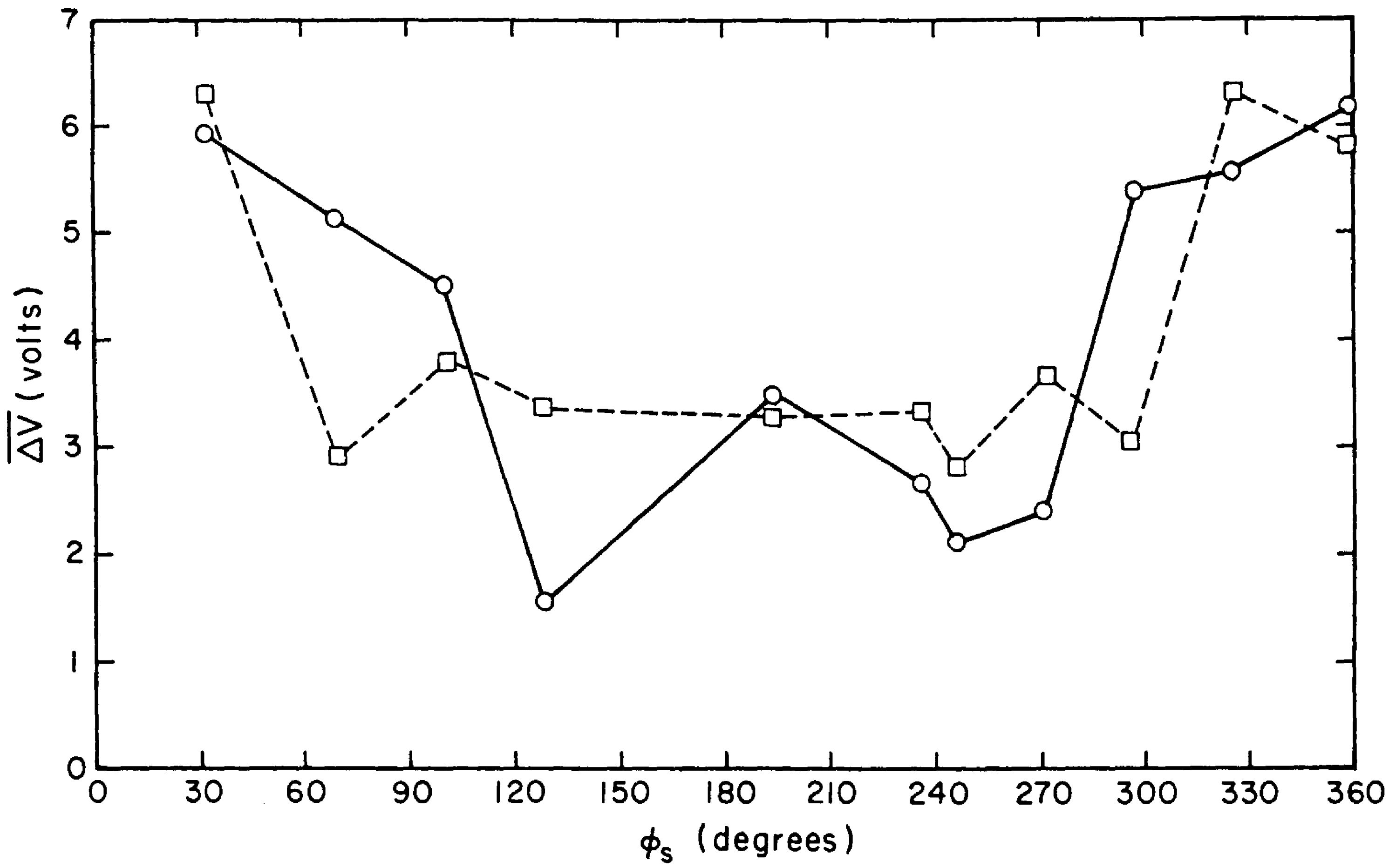

Figure 36. Same as figure 33 for cloud 4.

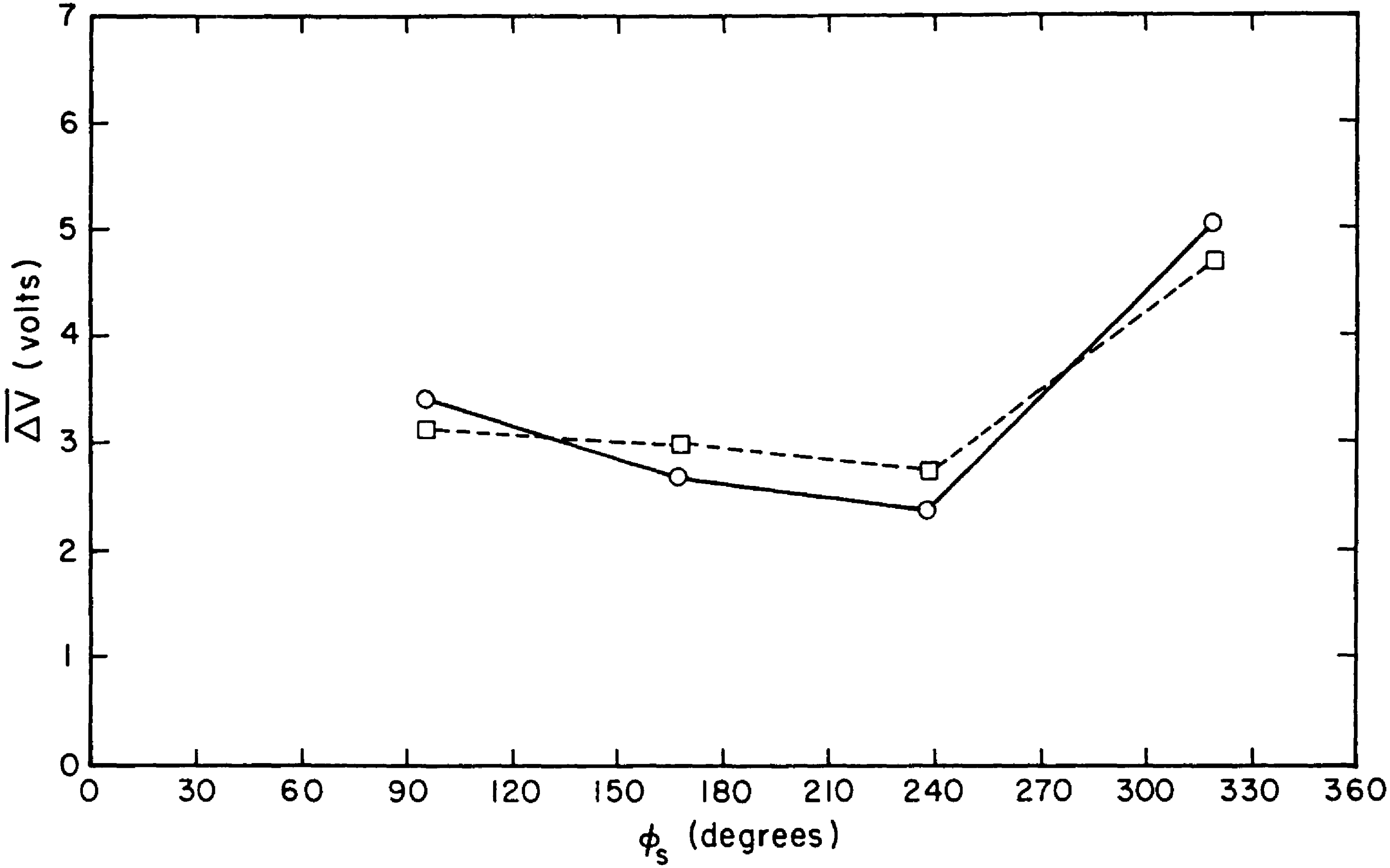

Figure 37. Same as figure 33 for cloud 5.

of the average of each radiometer scan would be equal to the sum of the corresponding model radiances. Each of the model radiances for a particular cloud was multiplied by the same normalization factor. With the exception of cloud 1 where no scans were taken on the solar side of the cloud, the averages of the radiometer scans have the same general shape as the model radiances around each cloud. There is a maximum in $\overline{\Delta V}$ of the radiometer scans on the solar side of each cloud. The difference between the brightest point on the solar side and the darkest point on the antisolar side of clouds 2-5 is about the same for the model radiances and the radiometer scans. There is even some indication of a small maximum in $\overline{\Delta V}$ of the radiometer scans of clouds 1 and 2 when ϕ_s is between 80° and 120°, although there are not enough points around each cloud to determine if this is due to smaller scale features since it does not appear in all the clouds. Clouds 1, 2 and 4 show a maximum in $\overline{\Delta V}$ of the radiometer scans on the antisolar side which is much sharper than the model predicts. This is again because the model radiances are averages over an entire cloud face.

In figures 33-37, the averages of the radiometer scans are within about one unit of the normalized model radiances for most of the positions around each cloud. There are a few radiometer points which are either much darker or much brighter than the normalized model radiance. The second scan from the right in figure 33, the first two scans from the left in figure 34 and the fourth scan from the left in figure 36 are all very much darker than the corresponding model radiances. All four of these scans passed through an area of the cloud which was shaded from above by another portion of the cloud. This results in a dark area on the cloud, especially on the solar side. All four of these points were on the three largest clouds. The second scan from the left and the third scan from the right in figure 36 are very much brighter than the corresponding model radiances. Both of these scans were taken at an angle of about 65° off from the direction of the incident solar beam. This area of the cloud was directly illuminated by the sun. At angles greater than 45° off from the incident solar beam, the scans were compared to model results from the X faces, as in figure 12. Since these faces are not directly illuminated by the sun, the model radiances are not as bright as those observed. This effect can also be seen in figure 35 at a ϕ_s of about 60° and in figure 34 at a ϕ_s of about 300°, but the difference between the radiometer scans and the model radiances are much less than the difference in figure 36. In figure 33, the model radiance and the average of the radiometer scan are about the same at a ϕ_s of 55°, and in figure 37, no scans were taken in the region where corner effects may have been important. The effect of the cloud corners then shows up strongly in only one of four cases, and only in a limited azimuth region.

In order to get a quantitative idea of how the model radiances and radiometer scans compare, a plot of the values of $\overline{\Delta V}$ of the radiometer scans versus the corresponding normalized model radiance was made and is shown in figure 38. If the model exactly predicted the average of the radiometer scans, all the points shown should lie along the diagonal line through the origin. A linear regression of the 44 points in figure 38 resulted in a correlation coefficient (r) of 0.64. In this case, the model radiances account for about 40 percent of the variance of the

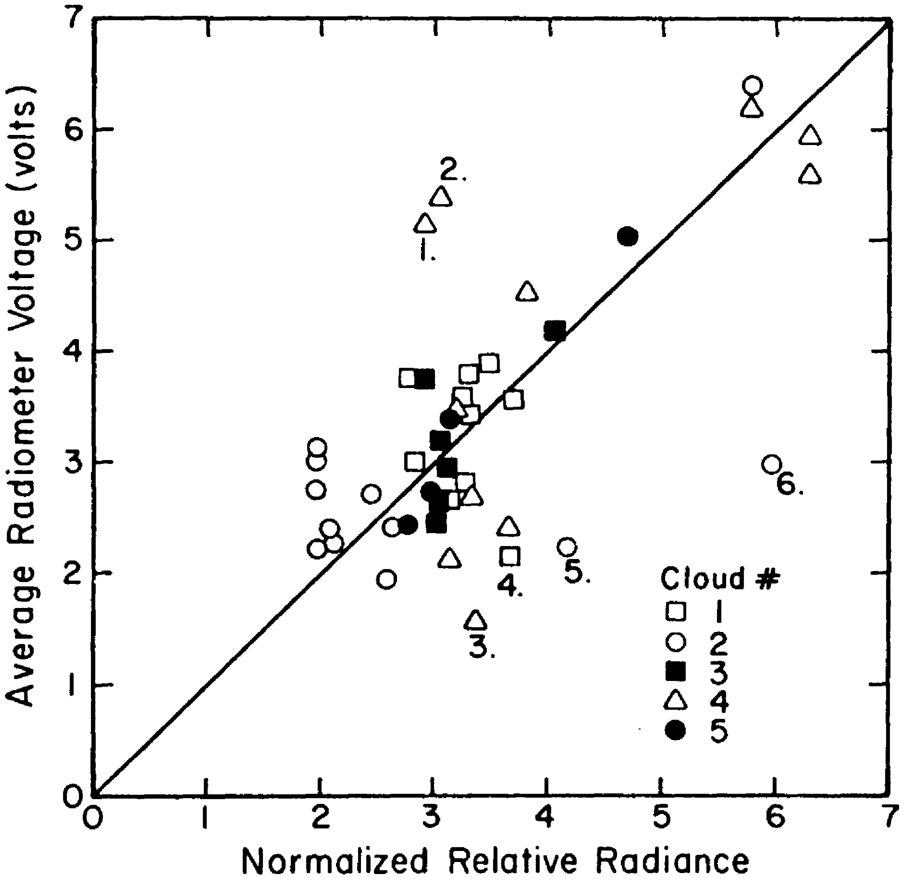

Figure 38. Average radiometer voltage versus normalized model radiance.

actual cloud radiances. This is about twice the variance accounted for by the correlation of the radiometer scans with the model radiances for cloud 2, where each scan was divided into about four or five sections. The value of the correlation coefficient for a linear regression is very sensitive to isolated points. In figure 38, the value of $\overline{\Lambda V}$ of the radiometer is much greater than the normalized model radiances for the points labelled 1 and 2. These are the two points from cloud 4 where the corner effects appeared to be important. The value of $\overline{\Lambda V}$ from the radiometer is much less than the normalized model radiances for points 3-6. These are the same four points previously discussed which passed through an area of the cloud which was shaded from above by another portion of the cloud. The radiometer scans of these six points reflect properties of the clouds which the model does not include. A linear regression which does not include these six points results in a correlation coefficient of 0.86. This indicates that about 75% of the variance of the actual cloud radiances are accounted for by the model. An interpretation of this is that on the scale of the average of a radiometer scan, the model radiances and radiometer scans agree very well, except in a few significant cases where the smaller scale cloud features and model corner effects are still important.

Since the radiometer scans were vertical, the averages of the scans were averages over a range of zenith angle. The average of a radiometer scan is still representative of only a limited range of azimuth angle. Increasing the field of view of the radiometer would actually be equivalent to an average over a larger range of zenith and azimuth angle. Increasing the azimuth angle should reduce the effect of the shaded portions of the cloud since these areas would be averaged with more cloud area which was not shaded. If the radiometer field of view were larger, the solar side of the cloud could be viewed at a ϕ_s greater than 45° in the model. The effect of the cloud corners would then be reduced. Since it was assumed that the radiometer was pointed at about the center of the cloud, and since the total field of view of the radiometer was only 2° and the cloud to radiometer distance was on the order of the cloud diameter, comparing scans to the solar side of the model at values of ϕ_s greater than 45° is not justified.

Since no horizontal cloud scans were taken, it is not possible to simulate increasing the radiometer field of view in the azimuthal direction. It is possible, however, to average over a larger horizontal area of the cloud by averaging successive scans together. For each cloud, the scans were divided into four groups, depending on which model cloud face they were compared to. All the scans in each group were averaged together and compared to the average of the corresponding model radiances. Figure 39 shows a plot of the average of each group of scans for each cloud versus the average of the corresponding model radiances. A linear regression of the 19 points in figure 39 resulted in a correlation coefficient of 0.91. The correlation in this case accounts for 83% of the variance. On this scale then, the model results compare well with the radiometer scans. It appears that as a larger portion of the cloud area is averaged over, the effects of the cloud shadows and model cloud corners become less significant.

The points in figure 39 are averages of from 1 to 4 radiometer scans. Assuming that the diameter of the spot size of the radiometer

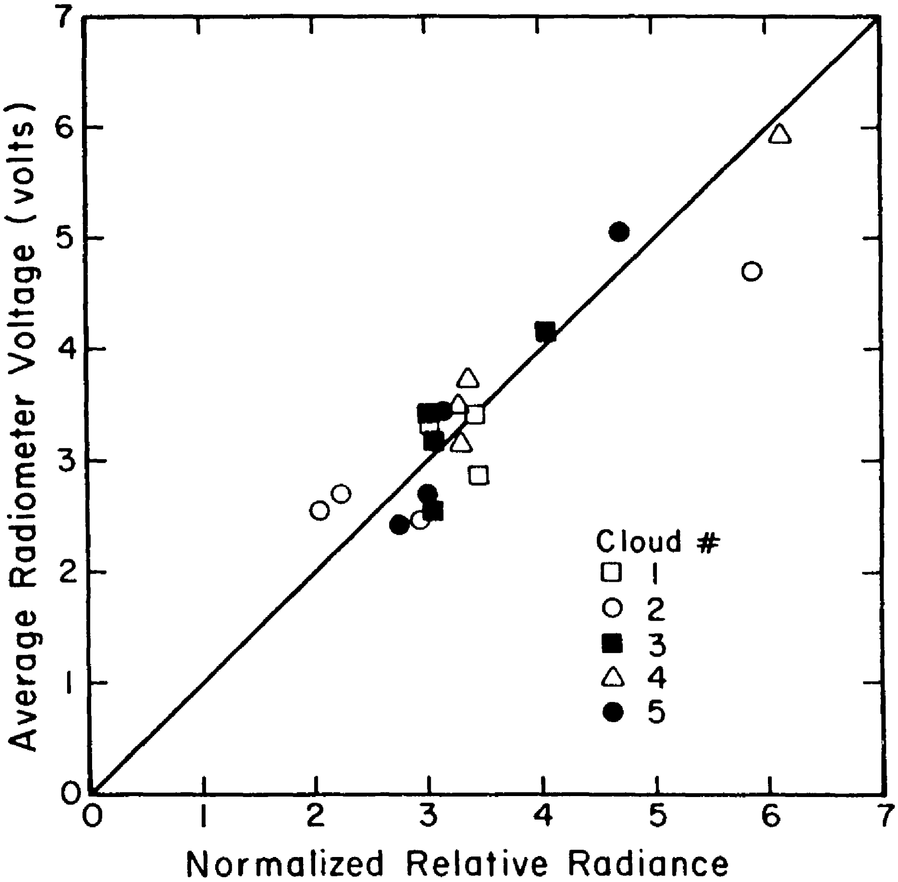

Figure 39. Average radiometer voltage of successive scans versus normalized model radiance.

was about 1/20 of the cloud height and the width to height ratio of each cloud was about 1.5, the radiometer viewed only about 1/600 of the area of a cloud side. Since each radiometer scan began at the middle of the cloud and ended at the cloud top, the average of a scan was an average over about 1/60 of the area of the cloud side. The average of 3 successive scans was an average over about 1/20 of the cloud side area. It is on the scale of about 1/20 of the area of a cloud side that the smaller scale features became less important, and the model results and radiometer scans compared well.

6.0 SUMMARY AND CONCLUSIONS

Relative radiances from a theoretical model for the scattering of solar radiation by finite clouds were compared to observed radiances from the sides of non-precipitating cumulus clouds. The sides of 5 cumulus clouds ranging from 1-3 km in depth were scanned with an aircraft mounted radiometer sensitive in the spectral range of 0.65 μm to 0.95 μm. Photographs of each cloud were taken just before each scan with a camera optically aligned with the radiometer. The theoretical model uses the Monte Carlo method of radiative transfer for finite clouds in the shape of rectangular parallelepipeds.

The agreement between the theoretical and observed radiances was strongly dependent on the area of the actual cloud side that was considered. The radiometer viewed a spot on each cloud with a diameter of about 1/20 of the cloud height, or about 1/600 of the total area of a cloud side. There was little correlation between the shape of a vertical radiometer scan and the corresponding model radiances. The shape of the radiometer scans was determined by the smaller scale cloud features which are not included in the model. The average of each radiometer scan was compared to the average of the corresponding model radiances. A linear regression of the model and observed relative radiances resulted in a correlation coefficient of 0.64. The low correlation was caused by a small number of observations where the model and actual radiances differed greatly due to smaller scale cloud features and to effects from the corners of the model cloud. The radiometer scans for each cloud were then divided into four groups, depending on which face of the model cloud they were compared to. The scans in each group were averaged together and compared with the corresponding model radiances. A linear regression of the model and actual radiances resulted in a correlation coefficient of 0.91 in this case. On this scale, the effects of the cloud corners and smaller scale cloud features became noticeably less important. These results verify the model calculations for cloud sides. The model cannot be used to predict the small scale radiance patterns of individual cumulus clouds. The small scale cloud features which are not included in the model have a large effect on the radiance variations of a cloud when viewed from a particular direction.

The variability of the radiance from the sides of the clouds was also studied. An upper limit for the relative radiance variations in the observed clouds was estimated from film density to be by a factor of between four and five for a resolution of about 10 m. Variations of radiance were less for the smaller clouds. The variation in radiance of the clouds gradually decreased as the diameter of the area viewed increased from 10 m to 800 m. There did not appear to be any critical size associated with changes in radiance. Most radiance variations were resolved on the scale of 100 m with the radiometer.

REFERENCES

Auer, A. H., 1967: A cumulus cloud design for continental airmass regimes. Journal de Recherches Atmospheriques, 3(3), 91-100.

Avaste, O. A. and G. M. Vainikko, 1976: A method of calculating radiative transfer in broken clouds. Paper presented at Symposium of Radiation in the Atmosphere, Garmisch-Partenkirchen, Germany held 19-28 August 1976.

Barkstrom, B. R. and R. F. Arduine, 1976: The effect of finite horizontal size of clouds upon the visual albedo of the earth. Paper presented at Symposium of Radiation in the Atmosphere, Garmisch-Partenkirchen, Germany, held 19-28 August 1976.

Brown, M. L., 1978: Digital-video manipulation of satellite imagery. Fourth Symposium on Meteorological Observations and Instrumentation, Denver, Colorado, April.

Busygin, V. P., N. A. Yevstratov and Ye. M. Feygelśon, 1973: Optical properties of cumulus and radiant fluxes for cumulus cloud cover. Atmos. Oceanic Phys., 9, 1142-1151.

Cashwell, E. D., and C. J. Everett, 1959: A Practical Manual on the Monte Carlo Method for Random Walk Problems. Pergamon Press, 153 pp.

Danielson, R. E., D. R. Moore and H. C. Van de Hulst, 1969: The transfer of visible radiation through clouds. J. Atmos. Sci., 26, 1078-1087.

Davies, R. and J. A. Weinman, 1976: Results from two models of the three dimensional transfer of solar radiation in finite clouds. Paper presented at Symposium of Radiation in the Atmosphere, Garmisch-Partenkirchen, Germany, held 19-28 August 1976.

Davies, R., 1978: The effect of finite geometry on the three-dimensional transfer of solar irradiance in clouds. J. Atmos. Sci., 35, 1712-1725.

Davis, John M., Stephen K. Cox and Thomas B. McKee, 1978: Solar absorption in clouds of finite horizontal extent. Paper presented at Third Conference on Atmospheric Radiation, Davis, California, held 28-30 June 1978.

Deirmendjian, D., 1969: Electromagnetic Scattering on Spherical Polydispersions. American Elsevier, 290 pp.

Griffith, C. G. and W. L. Woodley, 1973: On the variation with height of the top brightness of precipitating convective clouds. Journal of Applied Meteorology, 12, 1086-1089.

REFERENCES continued

Kattawar, G. W., and G. N. Plass, 1971: Radiance and polarization of light reflected from optically thick clouds. Appl. Opt., 10, 74-80.

Klehr, J. T., and T. B. McKee, 1978: Simulated radiance patterns for MIE absorbing finite clouds. Atmospheric Science Paper #285, Colorado State University.

Lenoble, J. (ed.), 1977: Standard procedure to compute atmospheric radiation transfer in scattering atmosphere. International Association of Meteorology and Atmospheric Physics (IAMAP), Radiation Commission, Boulder, Colorado, July, 125 pp.

McKee, T. B., and S. K. Cox, 1974: Scattering of visible radiation by finite clouds. J. Atmos. Sci., 31, 1885-1892.

McKee, T. B., and S. K. Cox, 1976: Simulated radiance patterns for finite cubic clouds. J. Atmos. Sci., 33, 2014-2020.

McKee, T. B., and J. T. Klehr, 1978: Effects of cloud shape on scattered solar radiation. Monthly Weather Review, 106, 399-404.

Reynolds, D. W., T. B. McKee and K. S. Danielson, 1978: Effects of cloud size and cloud particles on satellite-observed reflected brightness. J. Atmos. Sci., 35, 160-164.

Twomey, S., 1976: Computations of the Absorption of solar radiation by clouds. J. Atmos. Sci., 33, 1087-1091.

Warner, J., 1969: The microstructure of cumulus cloud. Part I General features of the droplet spectrum. J. Atmos. Sci., 26, 1049-1059.

Wendling, P., 1977: Albedo and reflected radiance of horizontally inhomogeneous clouds. J. Atmos. Sci., 34, 642-650.

BIBLIOGRAPHIC DATA SHEET	1. Report No. CSU-ATSP-313	2.
		3. Recipient's Accession No.

4. Title and Subtitle

A Comparison of Theoretical and Observed Radiances from Non-Precipitating Cumulus Clouds

5. Report Date May, 1979

6.

7. Author(s)

Mark DeMaria and Thomas McKee

8. Performing Organization Rept. No. CSU-ATSP-313

9. Performing Organization Name and Address

Colorado State University
Atmospheric Science Department
Foothills Campus
Fort Collins, CO 80523

10. Project/Task/Work Unit No.

11. Contract/Grant No.
GARP, GATE Project,
Grant ATM76-80568

12. Sponsoring Organization Name and Address

National Science Foundation

13. Type of Report & Period Covered

14.

15. Supplementary Notes

16. Abstracts

Relative radiances from a theoretical model for the scattering of solar radiation by finite clouds were compared to observed radiances from the sides of non-precipitating cumulus clouds. The sides of 5 cumulus clouds ranging from 1-3 km in depth with width to depth ratios of about 1.5 were scanned with an aircraft mounted radiometer sensitive in the spectral range of 0.65 to 0.95 μm. Photographs of each cloud were taken just before each scan with a camera optically aligned with the radiometer. The theoretical model uses the Monte Carlo method of radiative transfer for finite clouds in the shape of rectangular parallelepipeds. The radiometer field of view intercepted a circular spot with a diameter of about 1/20 of the cloud height. On this scale the radiometer scans were strongly affected by small scale cloud features so that the model radiances which are averages over a smooth cloud face did not compare well. A linear regression between the model and actual relative radiances resulted in a correlation coefficient(r) of only 0.47. When each scan was averaged, the smaller scale cloud features became less important. A linear regression for scan averages resulted in a correlation

17. Key Words and Document Analysis. 17a. Descriptors

Radiative properties of clouds
Finite cloud scattering model
Model verification using observations
Radiance variations

17b. Identifiers/Open-Ended Terms

17c. COSATI Field/Group

18. Availability Statement	19. Security Class (This Report) UNCLASSIFIED	21. No. of Pages 83
	20. Security Class (This Page) UNCLASSIFIED	22. Price

16. Abstract continued:

coefficient of 0.64. On this scale, the model calculations were verified by the observations except cloud corners were important. Elimination of the data points related to cloud features not contained in the model resulted in a correlation coefficient of 0.86. When several successive scans were averaged together, the correlation coefficient increased to 0.91. On this scale, the effects of the smaller scale cloud features and model cloud corners became noticeably less important.

The variability in relative radiance from the sides of the clouds were also studied. An upper limit for the relative radiance variations in the observed clouds was estimated from film density to be by a factor of between four and five. Variations of radiance were less for the smaller clouds. The radiance variations of the clouds gradually decreased as the diameter of the area viewed increased from 10 m to 800 m. Most radiance variations were resolved on the scale of 100 m with the radiometer.